Journal Pre-proofs

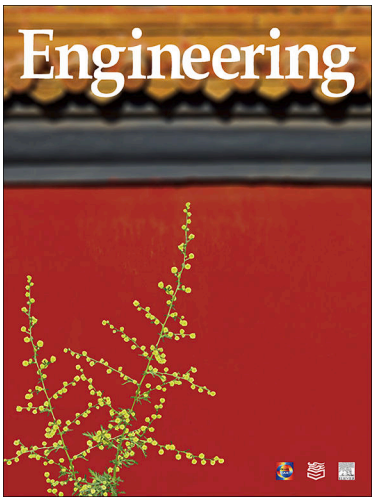

Article

UDAMSR Net: An Unsupervised Degradation-Aware Network for Enhancing the Spatial Resolution of Spectral Images for Crop Sensing

Weijie Tang, Ruomei Zhao, Hong Sun, Minzan Li, Lang Qiao, Mingjia Liu, Guohui Liu, Yang Liu, Di Song

PII: S2095-8099(26)00168-2
DOI: https://doi.org/10.1016/j.eng.2026.01.031
Reference: ENG 2294

To appear in: *Engineering*

Received Date: 8 October 2024
Revised Date: 30 December 2025
Accepted Date: 5 January 2026

Please cite this article as: W. Tang, R. Zhao, H. Sun, M. Li, L. Qiao, M. Liu, G. Liu, Y. Liu, D. Song, UDAMSR Net: An Unsupervised Degradation-Aware Network for Enhancing the Spatial Resolution of Spectral Images for Crop Sensing, *Engineering* (2026), doi: https://doi.org/10.1016/j.eng.2026.01.031

Research

Agricultural Sensors—Article

UDAMSR Net: An Unsupervised Degradation-Aware Network for Enhancing the Spatial Resolution of Spectral Images for Crop Sensing

Weijie Tang [a], Ruomei Zhao [a], Hong Sun [a,b,*], Minzan Li [a,b], Lang Qiao [c], Mingjia Liu [b], Guohui Liu [b], Yang Liu [a], Di Song [d]

[a] *Key Lab of Smart Agriculture Systems (MOE), China Agricultural University, Beijing 100083, China*

[b] *Key Laboratory of Agricultural Information Acquisition Technology (MARA), China Agricultural University, Beijing 100083, China*

[c] *Department of Bioproducts and Biosystems Engineering, University of Minnesota, Saint Paul, MN 55108, USA*

[d] *Department of Agricultural and Biological Engineering, University of Illinois at Urbana-Champaign, Urbana, IL 61801, USA*

* Corresponding author.

E-mail address: sunhong@cau.edu.cn (H. Sun)

ARTICLE INFO

Article history:

Received

Revised

Accepted

Available online

Keywords:

UDAMSR Net

Spatial resolution enhancement

Remote sensing image

Crop phenotyping

Crop sensing

Transfer learning

ABSTRACT

Low spatial resolution (LR) remote sensing data is widely adopted because of its lower cost, although its limited analytical precision constrains its full use in precision agriculture. By contrast, the acquisition of high spatial resolution (HR) data often requires substantial expense. To address this limitation, this study proposes an unsupervised degradation-aware multi-channel super-resolution network (UDAMSR) to enhance LR spectral images without requiring paired HR–LR training data. The main contributions are as follows: ① the original framework is extended with dedicated queue and reconstruction layers to process multispectral and hyperspectral image (HIS) cubes, and a contrast-learning-based degradation-aware module is integrated to address unknown real-world degradation; ② comprehensive evaluation is conducted using image quality metrics, spectral consistency analysis, and performance in crop remote sensing tasks, such as chlorophyll content estimation; ③ the generalization capability of the model is assessed using data from three imaging devices, two spatial scales (near-ground and unmanned aerial vehicle (UAV)), and two geographic regions. The results show that the proposed method achieves the best overall performance in the comprehensive evaluation, with a mean peak signal-to-noise ratio ($\overline{\text{PSNR}}$) of 32.78, a mean root mean squared error ($\overline{\text{RMSE}}$) of 6.93, a mean structural similarity index ($\overline{\text{SSIM}}$) of 0.89, and a mean spectral angle mapper ($\overline{\text{SAM}}$) of 0.131. The method effectively reduces the degradation in chlorophyll detection accuracy caused by spatial resolution reduction. The evaluation of generalization capability further shows that the proposed method demonstrates strong generalization across different spatial scales, geographic regions, devices, and data types. These results indicate that UDAMSR provides a robust, efficient, and cost-effective software solution that can compensate for hardware limitations and support high-quality crop phenotyping detection in diverse application scenarios.

1. Introduction

Crop phenotyping refers to the quantitative characterization of anatomical, physiological, and biochemical properties, as well as interactions with the environment, and chlorophyll content represents a key component of crop phenotyping [1]. Spectral imaging, commonly applied in proximal and remote sensing, provides an efficient approach for crop assessment because electronic transitions associated with molecular vibrations and chemical bond absorption are strongly related to chlorophyll, nitrogen, and other nutrient contents in the visible and near-infrared (Vis–NIR) region [2]. Over recent decades, spectroscopic imagery has been widely applied to determine crop nutritional status [3–5], in response to increasing food demand and the growing pressure on arable land productivity [6,7]. However, estimation accuracy remains constrained by limited data quality, which requires high spatial resolution (HR) remote sensing images as reliable data support [8]. Therefore, current research emphasizes spatial resolution enhancement of spectral images, with particular attention to super-resolution (SR) reconstruction architectures that improve original data quality and chlorophyll-based crop estimation performance.

To examine the limitations of low spatial resolution (LR) images in crop remote sensing monitoring, this study reviews commonly used spectral imaging equipment, constraints associated with LR data in crop sensing tasks, and limitations of existing HR image reconstruction methods, together with feasible solutions. Relevant methodological advances from broader remote sensing applications are also considered, including image classification [9], adaptive system optimization [10], unsupervised domain adaptation [11,12], and signal filtering [13]. This analysis clarifies the research direction and the associated methodological innovation.

1.1 Spectral imagery and constraints of low resolution for crop sensing

Spectral imaging for crop remote sensing mainly relies on three data types: color images, multispectral images (MSI), and hyperspectral images (HSI). Color images, because of their low cost and HR, are widely used for tasks related to morphological characteristics, such as weed identification [14], lodging classification [15], and above-ground biomass estimation [16] in potato crops. However, restriction to three spectral bands limits their capability for diagnosing internal crop nutrient status. MSI and HSI enable estimation of internal nutrient content [17–21], and early disease detection [22] through additional spectral information. These spectral advantages are associated with trade-offs, as an increasing number of spectral bands typically result in reduced spatial resolution, substantially higher costs, and lower resistance to interference [23,24]. This limitation originates from a fundamental hardware constraint, illustrated in Fig. 1, which shows the trade-off among spatial resolution, number of spectral bands, and cost. Researchers must therefore balance high spatial detail and rich spectral information, as achieving both simultaneously is often expensive. In addition, due to the imaging principles of fixed-focal-length systems (Eqs. (1)–(3)), spatial resolution decreases markedly as imaging distance increases, which affects all imaging modalities.

$$\frac{1}{f} = \frac{1}{u} + \frac{1}{v} \qquad (1)$$

$$h \approx \frac{H \cdot f}{u} (u \gg f) \quad (2)$$

$$h \propto \frac{1}{u}, A \propto \frac{1}{u^2} \quad (3)$$

where f is the focal length of the lens, u is the object distance, v is the image distance, and H, h, and A represent the actual height, image height, and image area of the captured subject, respectively.

LR substantially reduces the accuracy of crop remote sensing analyses by degrading critical spatial features [25], which limits applications such as species detection [26], and by reducing spectral heterogeneity [27], leading to failure of biodiversity monitoring indices [28]. Because major hardware advances remain challenging [29–31], this study emphasizes software-based approaches. Reconstruction of HR images from widely available LR-images has been validated in related applications, including vegetation cover mapping [32] and image conversion [33], and represents a practical strategy to compensate for hardware constraints and improve downstream tasks such as crop detection and classification [34].

Table 1
Different types of images for near-ground crop detection.

Type	Describe	Application	Reference
Color images	Nikon D700, RGB, handheld, 2272 × 1704, snapshot	Weeds identification	[14]
	Canon Power Shot SX170 IS, RGB, handheld, 4608 × 3456, snapshot	Lodging classification (sugarcane)	[15]
	DJI Phantom 4 Pro, RGB, UAV, 5472 × 3648, snapshot	Above-ground biomass estimation (potato)	[16]
MSIs	RedEdge-MX, 5 bands, UAV, 1280 × 960, snapshot	Leaf area index, chlorophyll estimation (corn)	[18]
	XIMEA XiQ, 25 bands, handheld 409 × 216, snapshot	Chlorophyll detection (wheat)	[19]
	Micasense ALTUM, 5 bands, UAV, 2064 × 1544, snapshot	Nitrogen estimation (wheat)	[17]
HSI	Micro-Hyperspec VNIR E, 400–1000 nm, UAV, 342 bands, 1.6 nm, 1024 lines external scan	Leaf nitrogen estimation (almond)	[20]
	SPECIM IQ, 400–1000 nm, handheld, 204 bands, 7 nm, 512 × 512 built-in line scan	Chlorophyll detection (wheat)	[21]
	SPECIM FX10, 400–1000 nm, handheld, 224 bands, 5.5 nm, 1024 lines external scan	Crown rot disease diagnosis (maize)	[22]

UAV: unmanned aerial vehicle; RGB: red, green, and blue.

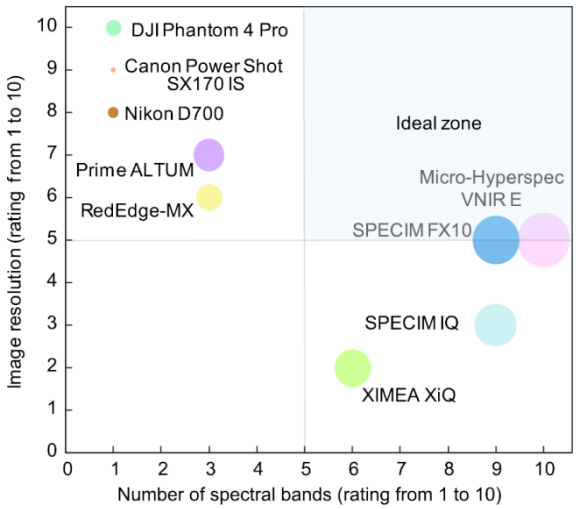

Fig. 1. Rating of imaging equipment commonly used for remote sensing of crop phenotypes (larger circular area indicates higher cost).

1.2. Existing methods and challenges in HR image reconstruction

Pan-sharpening is a mainstream SR approach in remote sensing that enhances spatial resolution by integrating panchromatic (PAN) images with MSI or HSI [35]. Although advanced algorithms such as Spectral Profile Partial Least-Squares (SP-PLS) [36], panchromatic-sharpening based on a generative adversarial network (Pan-GAN) [37], and surface- and deep-level constraint-based panchromatic-sharpening network (SDPNet) [38] have been developed, their application remains limited by the requirement for matched HR PAN images, which are often difficult to obtain in practice [39].

This constraint has motivated increasing interest in single-image super-resolution (SISR) techniques. Traditional SISR methods exist, but their performance is limited by the strongly nonlinear nature of the reconstruction problem and their sensitivity to noise [40]. Deep learning-based SISR methods have attracted considerable attention because of their strong representation learning ability and nonlinear modeling capacity [41–43]. Models such as very deep convolutional networks (VDSR) [44], deep sentinel-2 super-resolution network (DSen2) [45], deep residual squeeze and excitation network (DRSEN) [46], and embedded block residual network (EBPN) [47] achieve favorable performance when trained with sufficient high-quality HR–LR-image pairs or data generated using known degradation models. However, their practical deployment faces two major challenges. First, authentic high-quality HR–LR training pairs are scarce in real remote sensing scenarios. Second, real-world image degradation processes are complex and often unknown. When the assumed degradation model does not match the actual degradation, model performance decreases substantially [48]. Addressing data scarcity and unknown degradation in real applications therefore remains a critical challenge.

Table 2
Existing SR algorithms and challenges.

Method	Type	Brief description	Challenge
SP-PLS	Traditional pan-sharpening	Segments the hyperspectral cube into spectral profiles and calibrates a model between pixels in a spectral profile and their corresponding panchromatic values	Requires paired HR PAN
Pan-GAN	Deep learning based pan-sharpening	An unsupervised generative adversarial framework for pan-sharpening that does not rely on ground truth during training	
SDPNet	Deep learning based pan-sharpening	A surface- and deep-level constraint-based network that uses unique feature maps to constrain similarity between pan-sharpened results and ground truth, reducing information distortion	
Contrast-Guided Image Interpolation	Traditional SISR	Generates binary contrast-guided decision maps to guide interpolation filtering, reducing computational complexity.	Insufficient nonlinear capability
VDSR	Deep learning based SISR	Uses a deep network with cascaded small filters to exploit large contextual regions and learns residuals with high learning rates	Requires a large number of HR–LR-image pairs for training
DSen2	Deep learning based SISR	Performs end-to-end upsampling using a convolutional neural network trained with lower-resolution data	Supervised training, degradation using a fixed degradation model
DRSEN	Deep learning based SISR	Uses a deep residual squeeze-and-excitation network to model channel dependencies and enhance feature representation	Requires a large number of HR–LR-image pairs for training

EBPN	Deep learning based SISR	Incorporates an attention mechanism to capture inter-channel feature differences and reconstruct images using multi-depth features	Requires a large number of HR–LR-image pairs for training

1.3. Possible solution ideas and our contributions

To address the dual challenges of limited high-quality training data and unknown degradation in remote sensing SR, this study draws on two promising strategies: transfer learning (TL) [49] and degradation-aware learning. TL reduces data scarcity by pretraining general models on abundant external datasets and subsequently fine-tuning them using limited domain-specific data [50]. This strategy has been successfully applied in several remote sensing tasks [51], including leaf chlorophyll content estimation [52], yield estimation [53], and vegetation cover estimation [54]. Degradation-aware methods, such as the degradation-aware super-resolution (DASR) network [55], address unknown degradation by identifying degradation characteristics through contrastive learning and have reported strong performance.

The underlying principles of these approaches continue to develop, enabling effective and innovative applications across a range of visual tasks. These include handling complex distortions [56,57], processing hyperspectral data [58,59], and improving network performance [60].

Motivated by these advances, we modify the DASR framework and propose an unsupervised degradation-aware multi-channel super-resolution network (UDAMSR) for reconstructing real multi-channel remote sensing images in the absence of HR–LR-image pairs. The proposed model improves adaptability by learning to discriminate diverse real-world degradation patterns through a contrastive learning-based degradation-aware module. In addition, dedicated queuing and reconstruction layers are designed for MSI and HSI cubes, extending SR capability to multi-channel data. To address the lack of remote sensing SR datasets, a TL dataset is constructed using field-collected data.

The proposed method is validated using field experimental data acquired from three imaging devices: near-ground hyperspectral cameras, near-ground multispectral cameras, and unmanned aerial vehicle (UAV)-borne multispectral cameras. The overall structure of this study is shown in Fig. 2 and comprises three components:

(1) Network training and core validation: Training and evaluation of the proposed network using near-ground hyperspectral data, assessment of SR performance from both image and spectral perspectives, and validation through chlorophyll content estimation.

(2) Cross-device generalization testing: Application of the trained network to LR near-ground MSI to reconstruct HR images, followed by evaluation of generalization performance through chlorophyll content estimation.

(3) Cross-spatial scale and geographic generalization testing: Application of the trained network to LR UAV MSI collected across different geographic regions, followed by evaluation of generalization performance through chlorophyll content estimation.

To summarize this study, our contributions are:

(1) A novel unsupervised network: A DASR network is proposed to enhance the spatial resolution of remote sensing images without paired training data, reducing dependence on large labeled datasets.

(2) Comprehensive evaluation: SR performance and spectral consistency are systematically evaluated, and practical applicability in crop remote sensing is validated through chlorophyll content detection.

(3) Extensive validation of generalization capability: Strong adaptability is demonstrated across three imaging devices, two spatial scales (near-ground and UAV-based), and two geographic regions.

(4) Practical software solution: Compared with hardware upgrades, the proposed approach provides an efficient and economical alternative for obtaining high-spatial-resolution imagery, supporting crop sensing and analysis in diverse application scenarios.

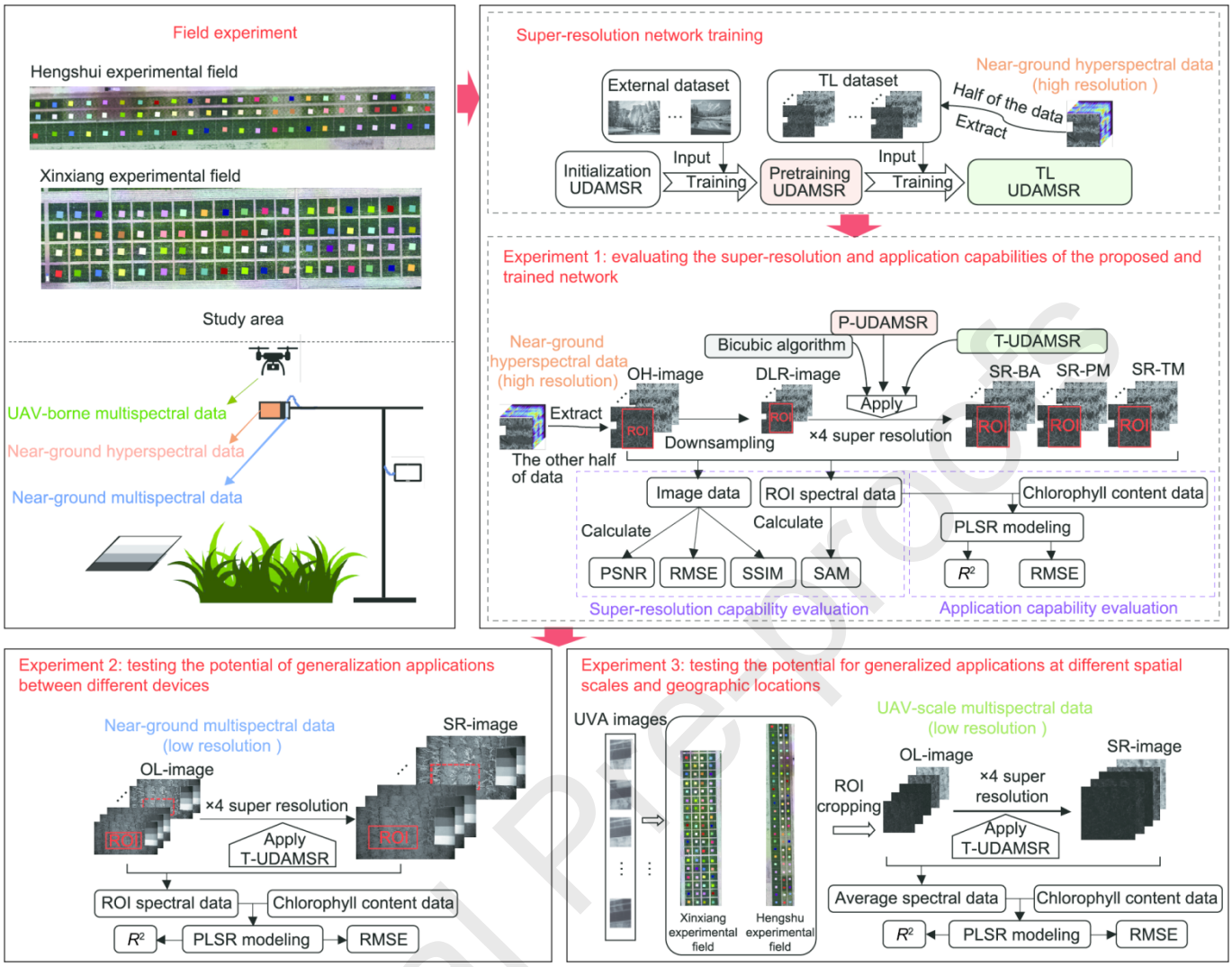

Fig. 2. The overall structure of this study. R^2: the coefficient of determination. PLSR: partial least squares regression. RMSE: root mean squared error; PSNR: peak signal-to-noise ratio; SSIM: structure similarity; SAM: spectral angle mapper; P-UDAMSR: pre-trained UDAMSR model; T-UDAMSR: transfer learning UDAMSR model; OH-image: original hyperspectral image; DLR-image: degraded low-resolution image. SR-BA: SR-image by traditional bicubic algorithm; SR-PM: SR-image by the P-UDAMSR model; SR-TM: SR-image by the T-UDAMSR model.

2. Methodology

2.1. Framework of UDAMSR

The overall framework of UDAMSR is illustrated in Fig. 3(a). It consists of an image degradation-aware network and a DASR network. The image degradation-aware network learns image degradation characteristics and provides degradation representations to the DASR network. The SR network performs spatial resolution enhancement of LR-images and is composed of five residual groups, each containing five degradation attention blocks (DABs).

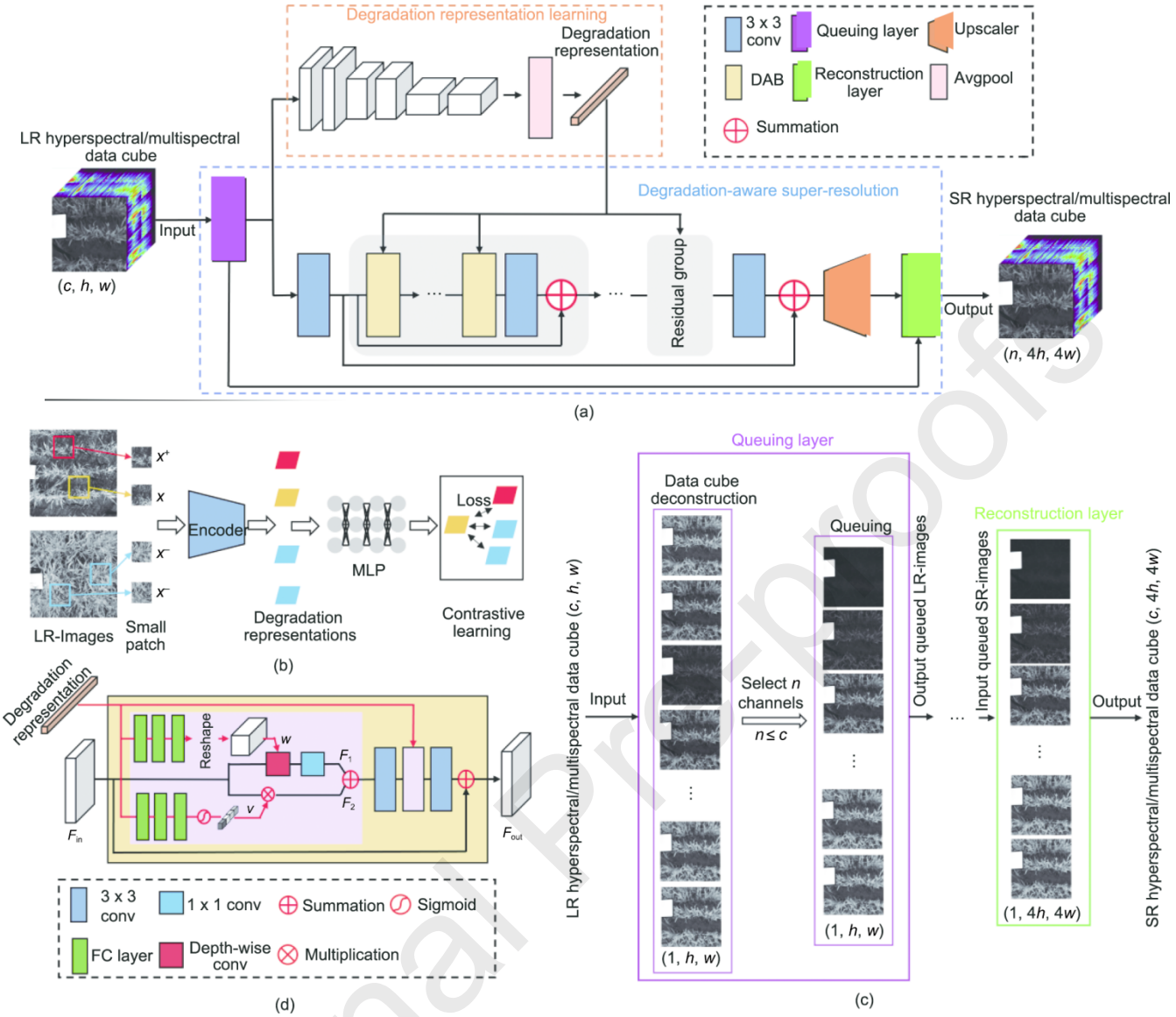

Fig. 3. UDAMSR network and key components. (a) The overall framework of UDAMSR. (b) Contrastive learning framework. (c) SR reconstruction. (d) Degradation awareness block. cov: convolution; x: small image cropped out of LR-image; x^+: positive sample, small image cropped out of LR-image; x^-: negative sample, small image cropped out of LR-image; c: channel; w: image width.

The end-to-end data processing workflow of this framework comprises the following steps:

(1) Data queuing: The input multispectral or hyperspectral data cubes are decomposed by the queuing layer into a sequence of grayscale images, which are organized into an input queue suitable for network processing.

(2) Degradation awareness: The degradation-aware network analyzes the input images and extracts a compact and informative degradation representation vector.

(3) SR reconstruction: The image sequence is fed into the main backbone of the SR network for deep feature extraction. Degradation-aware adaptive modulation is then applied by injecting the degradation representation vector into each DAB. Using the dual-branch structure of the DAB, feature modulation is performed jointly at the spatial and channel levels. The modulated features are subsequently upsampled through an upsampling module to reconstruct a series of HR grayscale images.

Data cube reconstruction: The reconstruction layer reassembles the output sequence of HR grayscale images to generate a high-quality, HR multispectral or hyperspectral data cube.

2.1.1. Degradation representation learning

Contrastive learning aims to learn discriminative feature representations by maximizing similarity between positive sample

pairs and minimizing similarity between negative sample pairs. This strategy focuses on differences in the abstract feature space rather than pixel-level differences, thereby avoiding complex pixel-domain operations and reducing computational complexity. The effectiveness of contrastive learning has been demonstrated in previous studies [61]. Based on the original DASR contrastive learning framework, the encoder input was modified from three-channel RGB images to single-channel grayscale images, as shown in Fig. 3(b). This adjustment allows the network to learn degradation features directly from grayscale images, avoiding efficiency loss caused by channel duplication while retaining the advantages of the original contrastive learning mechanism.

In this framework, two small patches are randomly cropped from each image. Patches extracted from the same image form a positive pair, whereas patches from different images form negative pairs. All patches are encoded, and degradation representations are learned through a three-layer fully connected network. Through unsupervised contrastive learning, the network distinguishes different degradation patterns and provides degradation characterization information to the SR network, enabling more effective reconstruction. The loss function of the degradation-aware network, denoted as $L_{\text{contrastive}}$, is shown in Eq. (4) as follows.

$$L_{contrastive} = \sum_{i=1}^{B} -log \frac{\exp\left(p_i^1 \cdot p_i^2 / \tau\right)}{\sum_{j=1}^{N_{queue}} \exp\left(p_i^1 \cdot p_{queue}^j / \tau\right)} \quad (4)$$

where B is the batch size, N_{queue} is the number of negative samples in the current queue, τ is the hyperparameter, p_i^1,p_i^2 are the two small patches cropped out of image i, which are positive samples, p_{queue}^j is the small patch cropped out of image j, which is a negative sample.

2.1.2. Multi-channel feasibility modification

The spectral image data used in this study include 25-channel near-ground MSI stored as single files, 5-channel UAV MSI stored as separate files for each channel, and 204-channel near-ground HSI stored as single files. The DASR network [55] was originally designed for natural RGB images and cannot be directly applied to MSI and HSI data cubes, which contain tens to hundreds of channels. Processing multi-channel data remains a key challenge in related research areas, such as multispectral polarimetric reflectance analysis [62], cross-scenario visual odometry [63], remote sensing land use monitoring [64], unstructured environment ground extraction [65], and video SR [66]. To enable SR reconstruction of MSI and HSI data, targeted modifications were introduced to the DASR framework based on the characteristics of multi-channel spectral images.

First, a queuing layer and a reconstruction layer were designed to process MSI and HSI data cubes, as shown in Fig. 3(c). The queuing layer decomposes MSI and HSI cubes into grayscale images that can be processed by the network and organizes them into an input queue. The reconstruction layer receives the sequential grayscale outputs from the network and reconstructs them into multispectral or hyperspectral data cubes.

Second, the DAB in DASR was optimized for grayscale image processing. Convolutional operations and feature extraction modules were adjusted to match grayscale data characteristics, and redundant components designed for RGB inputs were removed to focus on core grayscale features. The structure of the optimized DAB is shown in Fig. 3(d). The DAB receives degradation representations from the contrastive learning module and processes them through two branches. In the first branch, the degradation representation passes through three fully connected layers, is reshaped into a convolution kernel W(1×1×3×3), then W is deeply convolved with the input feature F_{in} and then passed through a 1×1 convolution layer to get the feature F_1. The other branch also passes through three fully connected layers and then passes through sigmoid activation to generate the channel-level modulation coefficients v, which is scaled to different feature channels of F_{in} to get the feature F_2. Finally, the features of F_1 and F_2 are summed up and sent to the subsequent layers to generate the output feature F_{out}.

3. Experiments

3.1. Field experiment and data acquisition

3.1.1. Study area

Field experiments were conducted at two sites: the Dryland Farming Institute, Hebei Academy of Agriculture and Forestry Sciences, located in Hengshui, Hebei Province, China, and the Xinxiang Comprehensive Experimental Base of the Institute

of Plant Protection, Chinese Academy of Agricultural Sciences, located in Xinxiang, Henan Province, China, as shown in Fig. 4(a).

At the Hengshui site, winter wheat was planted over a total area of 0.4 ha. Six nitrogen fertilizer application levels were established: A1, nitrogen 0 kg·ha^{-1}; A2, nitrogen 90 kg·ha^{-1}; A3, nitrogen 180 kg·ha^{-1}; A4, nitrogen 360 kg·ha^{-1}; A5, nitrogen 540 kg·ha^{-1}; and A6, nitrogen 720 kg·ha^{-1}. Each nitrogen level was replicated 12 times, resulting in 72 experimental plots. Measurements were conducted at the center of each plot, which was marked with signboards, and high-precision Global Positioning System (GPS) was used to record the latitude and longitude of each data collection point.

At the Xinxiang site, winter wheat was planted over a total area of 0.6 ha, with 72 experimental plots under identical fertilization conditions. Measurements were conducted at the center of each plot, marked with signboards, and high-precision GPS was used to record the geographic coordinates of the data collection points.

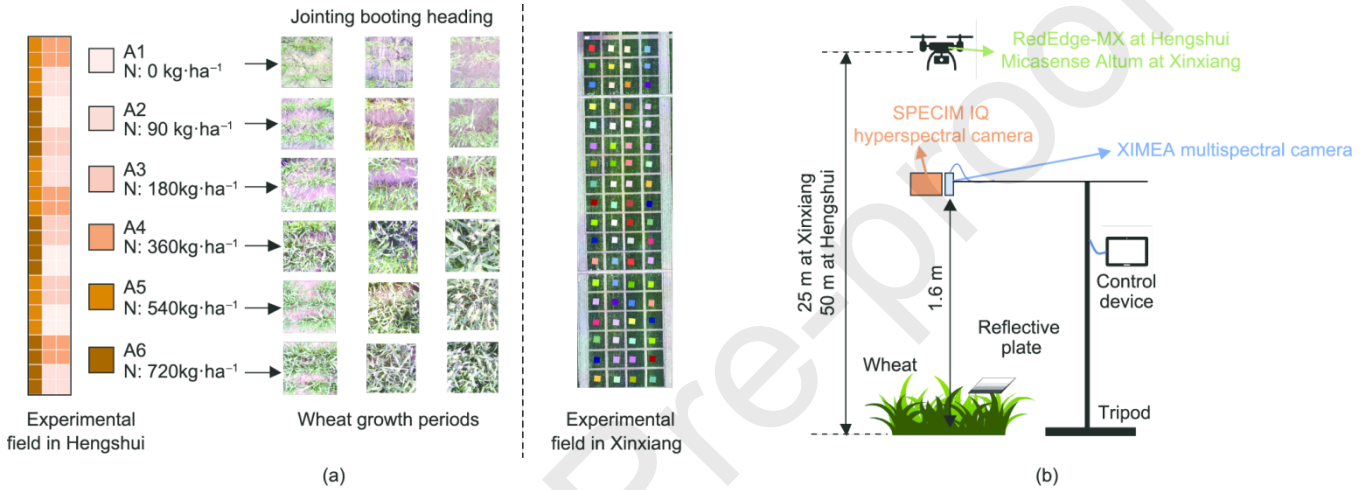

Fig. 4. Study area and remote sensing image acquisition. (a) Study area. (b) Remoting sensing image acquisition. N: nitrogen.

3.1.2. Remote sensing image acquisition

Remote sensing images at the Hengshui site were collected on March 29, April 22, and May 10, 2021, between 11:00 and 13:00, when the solar elevation angle was high. During these campaigns, wheat was at the jointing, booting, and heading stages, respectively. Across these growth stages, wheat exhibited rapid development and significant changes in canopy condition. Near-ground remote sensing images were acquired using a SPECIM IQ hyperspectral camera (SPECIM, Finland) and an XIMEA XiQ multispectral camera (XIMEA GmbH, Germany). UAV-scale images were collected using a DJI M600 Pro (DJI, China) equipped with a RedEdge-MX multispectral camera (MicaSense, USA). As shown in Fig. 4(b), the hyperspectral and multispectral cameras were mounted on a tripod, with the lens positioned 1.6 m above the ground to capture a broader canopy view. Based on the characteristics of the Hengshui experimental field, the UAV flight altitude was set to 50 m.

A reflective white board with a nominal reflectance of 95% was placed at canopy height for calibration of SPECIM IQ HSI. A four-level reflective board with nominal reflectance values of 5%, 25%, 50%, and 90% was used for calibration of XIMEA XiQ MSI. Three reflective fabrics with nominal reflectance values of 10%, 30%, and 70% were deployed for calibration of RedEdge-MX UAV MSI. For each acquisition date, 72 sets of near-ground HSI, 72 sets of near-ground MSI, and one set of UAV multispectral global images were obtained. In total, 216 sets of near-ground HSI, 216 sets of near-ground MSI, and three sets of UAV MSI were collected. Half of the near-ground HSI were used to construct a TL dataset for network training, whereas the remaining half was employed to evaluate the SR performance of the trained network and its application in chlorophyll content detection. The near-ground MSI and UAV MSI were used to assess the generalization capability of the trained network across different devices and spatial scales.

Remote sensing images at the Xinxiang site were collected on March 10, April 19, and May 7, 2022, between 11:00 and 14:00, when the solar elevation angle was high. Wheat was also at the jointing, booting, and heading stages during these campaigns. As shown in Fig. 4(b), data acquisition was conducted using a UAV equipped with a MicaSense Altum multispectral camera (MicaSense). The UAV flight altitude was set to 25 m based on the characteristics of the experimental field. Three reflective fabrics with nominal reflectance values of 10%, 30%, and 70% were placed in the field for MSI calibration. One set of UAV multispectral global images was collected during each campaign, resulting in three sets of UAV

MSI in total. These data were used to assess the generalization capability of the trained network across different geographic regions.

The parameters of the remote sensing image acquisition experiments are summarized in Table 3.

Table 3
Remote sensing image acquisition summary.

Parameter	Hengshui experiment	Xinxiang experiment
Date	Mar 29, Apr 22, May 10, 2021	Mar 10, Apr 19, May 7, 2022
Time	11:00–13:00	11:00–14:00
Wheat growth stage	Jointing, booting, heading	Jointing, booting, heading
Imaging platform & scale	Tripod (near-ground), UAV (aerial)	UAV (aerial)
Sensors	SPECIM IQ (hyperspectral), XIMEA XiQ (multispectral), RedEdge-MX (multispectral)	Micasense altum (multispectral)
Platform height	Tripod: 1.6 m; UAV: 50 m	UAV: 25 m
Calibration targets	SPECIM IQ: 95% white board; XIMEA XiQ: 5%, 25%, 50%, and 90% reflective board; RedEdge-MX: 10%, 30%, and 70% reflective fabrics	10%, 30%, and 70% reflective fabrics
Total data volume	216 Near-ground HSI; 216 near-ground MSI; 3 UAV MSI	3 UAV MSI
Purpose in this study	Network training & core validation; cross-device & cross-scale generalization	Cross-region generalization

Reflectance calibration of hyperspectral data was performed using the built-in calibration program of the SPECIM IQ camera. Reflectance calibration of near-ground multispectral data was conducted using MATLAB. For each image set, pixels corresponding to different reflectance levels of the reflective board were extracted, and calibration lines were fitted after assigning known reflectance values to correct all pixels in the image. Reflectance calibration of UAV MSI was performed using ENVI software. The stitched full-field map was imported into ENVI, three reflective fabric regions were manually selected and assigned reflectance values, and calibration lines were automatically fitted to correct all pixels across the entire image.

3.1.3 Chlorophyll data acquisition

Wheat canopy leaves were collected at the same locations as the spectral image acquisitions and placed in sample bags labeled with the corresponding plot serial numbers. Leaf chlorophyll content was then determined in the laboratory according to established procedures [19], as described below:

(1) Wheat leaves were cut and weighed to 0.4 g using a high-precision balance and placed in a test tube labeled with the corresponding serial number.

(2) A volume of 40 mL of 95% ethanol solution was added to the test tube. The wheat leaves were fully immersed, and the tube was sealed.

(3) Chlorophyll extraction was conducted under light-proof conditions for 48 h, with the tube shaken every 6 h until the leaves were completely discolored.

(4) The absorbance of the extraction solution at 649 and 665 nm was measured using a spectrophotometer (UV1800, Shimadzu Ltd., Japan).

(5) Leaf chlorophyll content was calculated using Eqs. (5)–(7).

$$C_a = 13.95 \times D_{665} - 6.88 \times D_{649} \quad (5)$$

$$C_b = 24.96 \times D_{649} - 7.32 \times D_{665} \quad (6)$$

$$C_t = C_a + C_b \quad (7)$$

where C_a is the content of chlorophyll a, C_b is the content of chlorophyll b, and C_t is the sum of chlorophyll content, mg·L^{-1}. D_{649} and D_{665} are the absorbance values of the extraction solution at 649 and 665 nm wavelength bands, respectively.

3.2. Data preparation for SR network training

3.2.1 External dataset

Because a sufficiently large collection of HR remote sensing images is not available for network training, a TL strategy was adopted. Instead of training the network directly on a limited target dataset, external datasets were first used for pretraining. Common SR training datasets in natural image SR include DIV2K and Flickr2K. Both datasets contain images with resolutions exceeding 2K. The DIV2K dataset includes 800 images, whereas Flickr2K contains 2650 images. These two datasets were combined to form a dataset of 3450 images. The original color images were converted to grayscale using Eq. (8), resulting in an external training dataset consisting of 3450 grayscale images.

$$\text{Gray} = 0.299 \times \text{Red} + 0.587 \times \text{Green} + 0.114 \times \text{Blue} \quad (8)$$

where Gray is the grayscale image and Red, Green, and Blue are the red, green, and blue channel images of the color image.

3.2.2 TL dataset

The TL dataset was constructed using field-collected HSI of wheat canopies. A total of 108 HSI sets were used, and ten spectral channels within the 650–900 nm wavelength range were extracted from each hyperspectral cube. This resulted in 1080 images, each with a spatial resolution of 512 pixels × 512 pixels.

3.3 SR network training

The UDAMSR network consists of two subnetworks: a degradation representation learning network and a SR network. The training procedure was divided into two stages. In the first stage, the degradation representation learning network was trained independently for 100 epochs. In the second stage, the entire network was trained in an end-to-end manner for 300 epochs.

To enrich degradation representations, anisotropic Gaussian kernels were applied to degrade the original images, followed by the addition of noise. The Gaussian kernel size was set to 21. The covariance matrix of the kernel was defined by random eigenvalues λ_1, λ_2, and random rotation angle θ. $\lambda_1$and λ_2 range from [0.1,4], θ range from [0, π], and the noise intensity ranges from [0,10].

Training was performed on a workstation equipped with an Intel Core i7-10875H processor and an NVIDIA GeForce RTX 2070S graphics card, running Ubuntu 22.04 LTS. The key hyperparameters used in the two-stage training process are summarized in Table 4.

For TL, the same training strategy as that used in pretraining was adopted. The pre-trained UDAMSR model is denoted as pre-trained UDAMSR model (P-UDAMSR), whereas the model obtained after TL is denoted as transfer learning UDAMSR model (T-UDAMSR). The overall training workflow is illustrated in Fig. 5(a).

Table 4
Training hyperparameters.

Hyperparameter	Stage 1: degradation representation training	Stage 2: whole network training
Epochs	100	300
Batch size	64	64
Optimizer	ADAM ($\beta_1 = 0.9, \beta_2 = 0.999$)	ADAM ($\beta_1 = 0.9, \beta_2 = 0.999$)
Initial learning rate	1×10^{-3}	1×10^{-4}
Learning rate schedule	Decreased by one order of magnitude every 60 epochs	Decreased to half every 125 epochs
Loss function	Eq. (4) (see Section 2.1.1)	$L = L_{\text{SR}} + L_{\text{contrastive}}$

	—	4
SR scale		
	—	L_{SR} is the L_1 loss between the SR-image and the original image
Remarks		

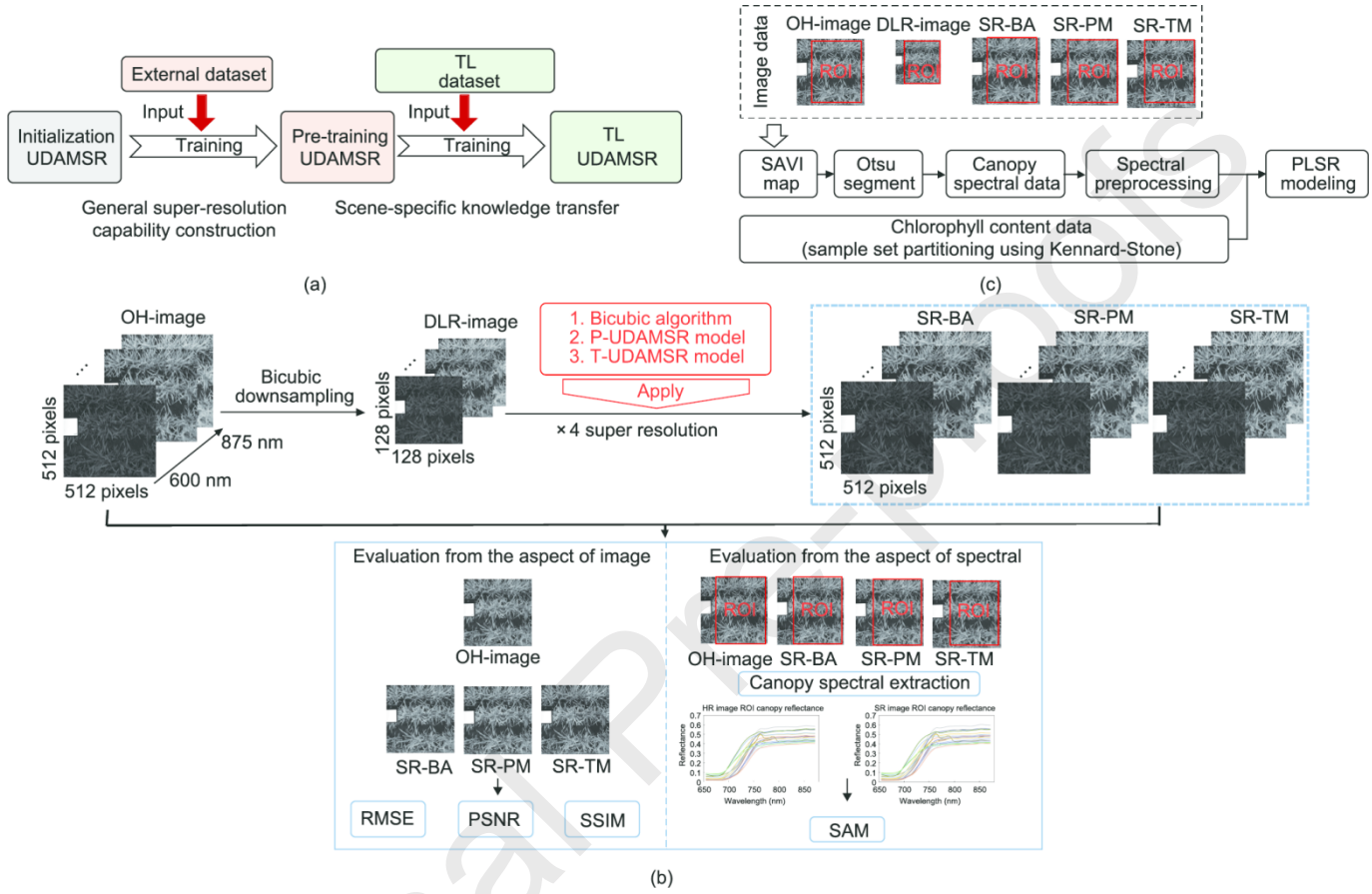

Fig. 5. Flowchart of model training and evaluation experiments. (a) Flowchart of model training. (b) Evaluation of Network SR capability. (c) Application experiment of chlorophyll content detection. SAVI: soil-adjusted vegetation index.

3.4. Evaluation of the trained neural network model

3.4.1. Data processing flow of SR ability evaluation experiment

The evaluation experiments used a subset of field-collected wheat canopy HSI that were not included in the training dataset. One dataset was selected for each fertilization level, resulting in 18 hyperspectral datasets covering three growth stages. The spatial resolution of the HSI was 512 pixels × 512 pixels, and the selected spectral range was 600–875 nm. The original HSI is denoted as the original hyperspectral image (OH-image), and the degraded LR-image obtained after degradation of the OH-image is denoted as the degraded low-resolution image (DLR-image). Python and MATLAB R2022b were used for data processing, and the workflow is illustrated in Fig. 5(b), as described below:

(1) To simulate LR conditions, the OH-image was degraded using a bicubic downsampling algorithm. The spatial resolution was reduced by a factor of four, from 512 pixels × 512 pixels to 128 pixels × 128 pixels, generating the corresponding DLR-image. This downsampling factor was selected to introduce a substantial resolution gap and to rigorously evaluate the reconstruction capability of SR models.

(2) The DLR-image was super-resolved to 512 pixels × 512 pixels using the traditional bicubic algorithm, the P-UDAMSR model, and the T-UDAMSR model. The resulting images are denoted as SR-image by traditional bicubic algorithm (SR-BA), SR-image by the P-UDAMSR model (SR-PM), and SR-image by the T-UDAMSR model (SR-TM), respectively.

(3) Root mean squared error (RMSE), peak signal-to-noise ratio (PSNR), and structural similarity index (SSIM) were

calculated for SR-BA, SR-PM, and SR-TM to evaluate model performance from the image perspective.

(4) Canopy spectra within the same region of interest (ROI) were extracted from the OH-image, SR-BA, SR-PM, and SR-TM, respectively, and spectral angle mapper (SAM) values were calculated to assess model performance from the spectral perspective.

3.4.2. Evaluation measures of the model's SR capability

Four commonly used metrics were applied to evaluate SR performance: RMSE, PSNR, SSIM, and SAM. PSNR, SSIM, and RMSE assess image enhancement performance from the spatial perspective, whereas SAM evaluates spectral consistency from the spectral perspective.

RMSE is the square root of the mean square error (MSE) and measures the difference between the SR-image and the HR image. RMSE is calculated using Equations (9) and (10), where S and H denote the SR-image and the HR-image, respectively, and m and n denote the size of the image. Smaller RMSE values indicate better model accuracy.

$$\mathrm{MSE} = \frac{1}{mn}\sum_{i=0}^{m-1}\sum_{j=0}^{n-1}[H(i,j) - S(i,j)]^2 \tag{9}$$

$$\mathrm{RMSE} = \sqrt{\mathrm{MSE}} \tag{10}$$

PSNR is an image quality metric based on the squared error between the HR image and the SR-image. It is calculated using Eq. (11), where B denotes the bit-depth of the image. Higher PSNR values indicate that the SR-image more closely approximates the HR image.

$$\mathrm{PSNR} = 10 \cdot \log_{10}\left(\frac{(2^B - 1)^2}{\mathrm{MSE}}\right) \tag{11}$$

SSIM is a full-reference image quality index that evaluates similarity from the perspectives of brightness, contrast, and structure. For 8-bit images, SSIM is calculated using Eq. (12), where μ_{H} is the mean of HR image, μ_{S} is the mean of SR-image, σ_{H}^2 and σ_{S}^2 are the variance of HR image and SR-image, respectively, and $2\sigma_{\mathrm{HS}}$ is the covariance of HR image and SR-image. SSIM is a number between 0 and 1. The larger the SSIM, the smaller the difference between the two images.

$$\mathrm{SSIM} = \frac{(2\mu_{\mathrm{H}}\mu_{\mathrm{S}} + 2.55^2)(2\sigma_{\mathrm{HS}} + 7.65^2)}{(\mu_{\mathrm{H}}^2 + \mu_{\mathrm{S}}^2 + 2.55^2)(\sigma_{\mathrm{H}}^2 + \sigma_{\mathrm{S}}^2 + 7.65^2)} \tag{12}$$

SAM, proposed by Kruse et al. in 1993 [67], treats the spectrum of each pixel as a high-dimensional vector and quantifies spectral similarity by computing the angle between two vectors. Smaller angles indicate greater spectral similarity. SAM is calculated using Eq. (13), where r_{H} is the spectral reflectance sequence of the ROI in the HR image and r_{S} is the spectral reflectance sequence of the ROI in the SR-image. The smaller the value of SAM indicates that the two spectra are more similar.

$$\mathrm{SAM} = \cos^{-1}\frac{r_H^T r_S}{\sqrt{r_H^T r_H}\sqrt{r_S^T r_} \tag{13}$$

3.4.3. Data processing flow for evaluating application effects of the SR model

Accurate estimation of chlorophyll content requires precise segmentation of the crop canopy from the soil background in

spectral images, which depends on HR. Therefore, chlorophyll content estimation was used as an application case to evaluate the practical effectiveness of the proposed network.

As shown in Fig. 5(c), the original HSI is denoted as the OH-image, the degraded LR-image as the DLR-image, and the SR-images as SR-BA, SR-PM, and SR-TM. The dataset was divided into calibration and validation subsets using the Kennard–Stone (KS) algorithm, which distributes samples evenly in the feature space. ROI background segmentation was performed using the Otsu method based on the soil-adjusted vegetation index (SAVI), and canopy spectra were subsequently extracted. SAVI was proposed by Huete to reduce soil background effects by introducing a soil adjustment factor L into the normalized difference vegetation index (NDVI) and is calculated using Eq. (14).

$$\mathrm{SAVI}(x,y) = \frac{(\mathrm{NIR}(x,y) - \mathrm{RED}(x,y))}{(\mathrm{NIR}(x,y) + \mathrm{RED}(x,y) + L)}(1 + L) \qquad (14)$$

where $\mathrm{SAVI}(x,y)$ is the SAVI value at pixel (x,y), $\mathrm{NIR}(x,y)$ is the reflectance value of the NIR channel pixel, $\mathrm{RED}(x,y)$ is the reflectance value of the red channel pixel, and L is the adjusting factor, which is usually taken as $L = 0.5$.

The extracted spectral data were preprocessed using the multiplicative scatter correction (MSC) algorithm, which reduces spectral variability caused by scattering differences and improves correlation between spectra and reference measurements.

The processed spectra were then used to construct a partial least squares regression (PLSR) model for chlorophyll content estimation.

3.4.4. Evaluation measures for application performance of the SR model

An application-oriented experiment was designed to evaluate whether SR processing improves chlorophyll content estimation accuracy. All 108 sets of field-collected wheat canopy HSI within the 600–875 nm range were used to construct a PLSR prediction model for chlorophyll content. Model performance was evaluated using RMSE and the coefficient of determination (R^2). RMSE is used to measure the dispersion of the results; the smaller the value, the more accurate the model. R^2 is used to measure how well the model fits; the closer the value of R^2 is to 1, the more accurate the model is.

4. Results

4.1. SR network training logs

Network training included pretraining and TL, and each phase comprised image degradation representation training and whole-network training. Loss values were recorded throughout the training process. During image degradation representation training, the loss function was $L_{\mathrm{contrastive}}$, and the loss of whole network training is $L = L_{\mathrm{SR}} + L_{\mathrm{contrastive}}$. In all cases, loss values showed a decreasing trend, and losses obtained during TL were consistently lower than those obtained during pretraining. For image degradation representation training, the pretraining loss decreased by 2.986, corresponding to a decrease rate of 51.4%, whereas the TL loss decreased by 3.63, corresponding to a decrease rate of 67.1%. The decrease rate during TL was therefore higher than that during pretraining. The loss trends for whole-network training differed between the two phases. During pretraining, the loss decreased rapidly in the first 30 epochs and then declined more gradually, with a total reduction of 2.727. In contrast, the initial loss during TL was already lower than the final loss achieved during pretraining. The loss then decreased slowly during training, with a total reduction of 0.45. The detailed loss variations during training are provided in Appendix Fig. S1.

4.2. Results of SR capability evaluation

4.2.1 Results of evaluation metrics for image perspective

To compare different SR methods, representative images from six fertilization levels were selected. Enlarged views of the OH-image, SR-BA, SR-PM, and SR-TM for wheat at the jointing stage were used as examples. The SR-BA images appear the most blurred, with substantial loss of edge information. By contrast, SR-PM and SR-TM images are clearer, and leaf edges can be more effectively distinguished from the background. The PSNR, RMSE, and SSIM results for SR-BA, SR-PM, and SR-TM are shown in Fig. 6. Across all fertilization levels, deep learning-based methods achieved better performance than the traditional bicubic algorithm for all three metrics. In addition, compared with the pre-trained model, the TL-based model achieved further improvement in PSNR, RMSE, and SSIM.

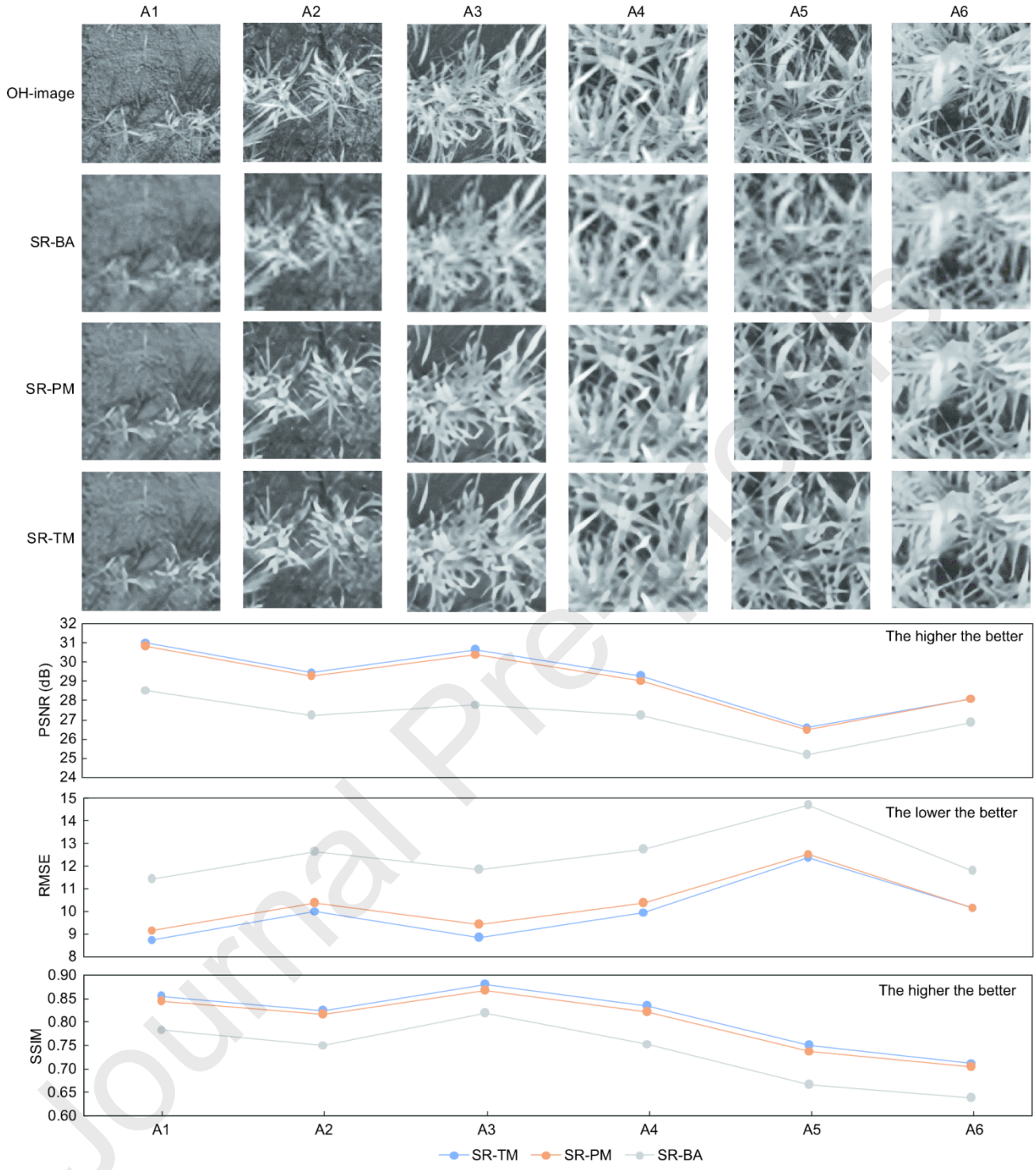

Fig. 6. Comparison of original and SR-images and image evaluation metrics under different fertilization levels in wheat at the jointing stage.

4.2.2. Evaluation results from the spectral perspective

Canopy reflectance spectra were extracted from the images, as shown in Fig. 7. Deviations between the super-resolved spectral curves and the original spectral curves were observed, and the magnitude of these deviations varied across fertilization levels. As fertilization level increased and canopy cover became denser, the super-resolved spectral curves became closer to the original curves. At the first three fertilization levels, the spectral curves of SR-TM were closest to the original spectra, whereas SR-BA exhibited the largest deviation. At the higher fertilization levels, the spectral curves from all methods became more concentrated.

Spectral similarity was further quantified using SAM values calculated between the spectra extracted from SR-BA, SR-

PM, and SR-TM and those from the original images. At fertilization levels A1–A2, where soil cover exceeded 70%, SAM values for SR-BA were significantly higher than those for the deep learning-based methods, indicating stronger spectral distortion under bicubic interpolation. The SAM values for SR-PM were also higher than those for SR-TM. At fertilization level A3, where canopy cover exceeded 50%, the SAM values of SR-BA and SR-PM were similar and both were substantially higher than those of SR-TM. At fertilization levels A4–A6, with canopy cover exceeding 70%, SR-PM exhibited the largest SAM values. SR-BA showed the lowest SAM values, whereas the SAM values of SR-TM were very close to those of SR-BA, with a maximum difference of 0.015. Across all fertilization levels, SR-TM showed more stable and overall superior performance.

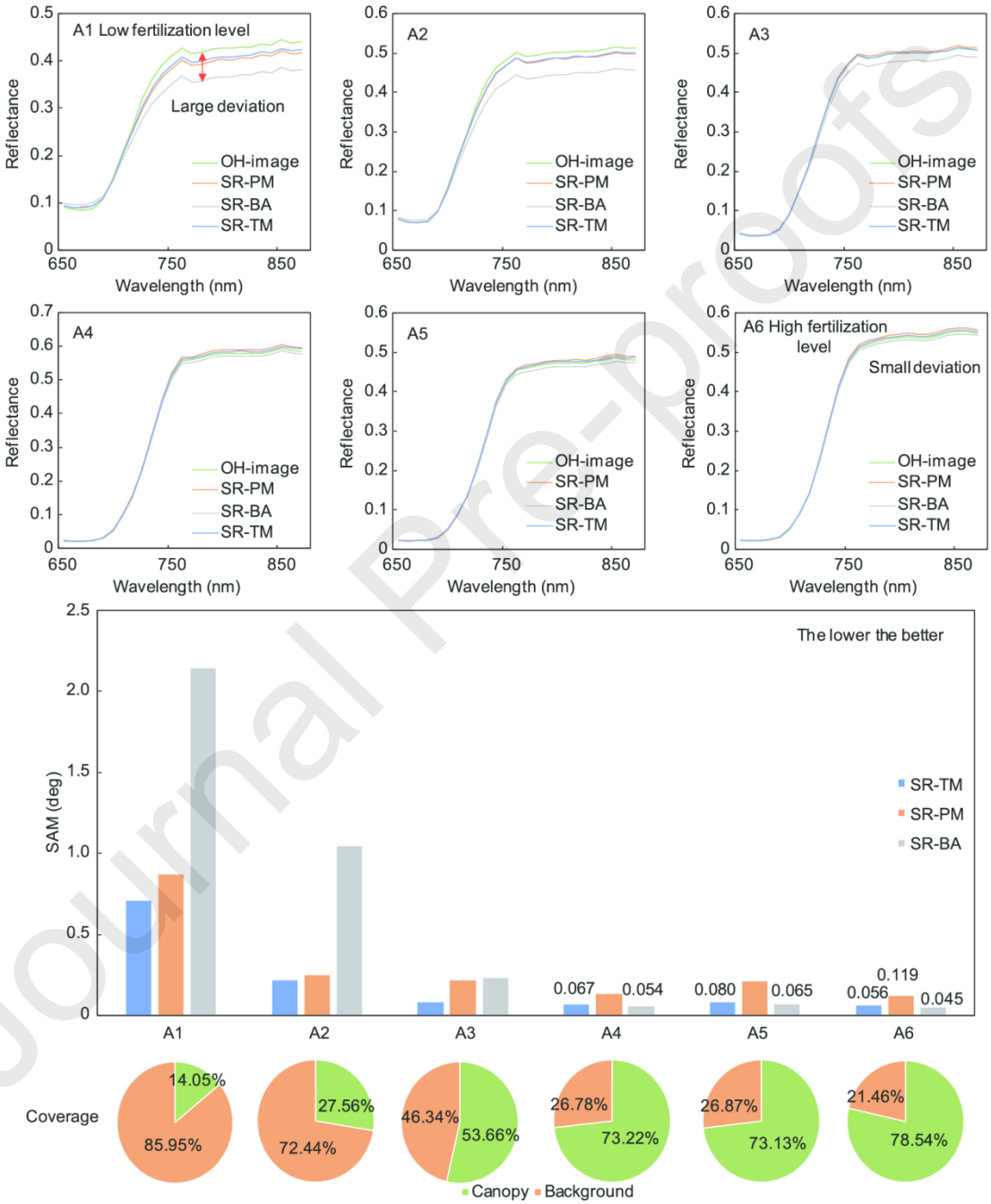

Fig. 7. Wheat canopy spectral reflectance, SAM values, and canopy cover at the jointing stage under different fertilization levels.

4.2.3. Summary of SR capability evaluation

The mean values of PSNR, RMSE, SSIM, and SAM across all samples are summarized in Table 5. The results indicate that the outputs reconstructed using the T-UDAMSR model achieve better and more stable performance from both image and

spectral perspectives. These findings demonstrate that the proposed model can efficiently reconstruct HR images from LR inputs using a cost-effective software-based approach.

Table 5
Mean values of PSNR, RMSE, SSIM, and SAM for all samples.

Data	$\overline{\text{PSNR}}$	$\overline{\text{RMSE}}$	$\overline{\text{SSIM}}$	$\overline{\text{SAM}}$
	30.16	9.24	0.83	0.372
SR-BA	32.48	7.21	0.88	0.163
SR-PM	32.78	6.93	0.89	0.131
SR-TM				

4.3. Results of the application effect of the SR model

4.3.1. Statistical results and partitioning of chlorophyll content data

Chlorophyll content data from 108 wheat leaf samples collected in the Hengshui experiment were analyzed. The statistical results are summarized in Table 6, which reports chlorophyll content for six nitrogen fertilizer application levels, three growth stages, and the calibration and validation subsets. Chlorophyll content increased with nitrogen application from A1 to A4 and then decreased at higher nitrogen levels (A5 and A6). Wider variability in chlorophyll content was observed at the jointing and heading stages. The calibration set included 72 samples with chlorophyll content ranging from 10.79 to 41.96 mg·L^{-1}, with a mean value of 27.62 mg·L^{-1}. The validation set included 36 samples with chlorophyll content ranging from 12.85 to 40.82 mg·L^{-1}, with a mean value of 28.76 mg·L^{-1}. The chlorophyll range of the validation set was fully contained within that of the calibration set, which supports the development of a reliable prediction model. Corresponding box plots are provided in Appendix Fig. S2.

Table 6
Statistical results of chlorophyll content and dataset partitioning.

Data	Number of samples	Max (mg·L^{-1})	Min (mg·L^{-1})	Mean (mg·L^{-1})	Median (mg·L^{-1})	Standard deviation
	18	23.69	11.55	16.18	14.96	3.71
A1	18	23.60	10.79	19.46	20.45	3.51
A2	18	31.71	12.38	24.66	26.54	5.45
A3	18	39.78	31.58	36.24	37.09	2.80
A4	18	40.89	29.67	35.20	34.68	3.53
A5	18	41.96	31.40	36.25	35.03	3.34
A6	36	38.87	10.79	26.67	29.97	8.86
Jointing	36	36.50	12.78	27.24	29.89	7.60
Booting	36	41.96	11.55	30.08	34.22	10.53
Heading	108	41.96	10.79	28.00	30.62	9.12
Total sample	72	41.96	10.79	27.62	29.97	9.31
Calibration set	36	40.82	12.85	28.76	32.36	8.80
Validation set						

4.3.2 Evaluation of chlorophyll content estimation performance

Segmentation was performed on OH-image data, DLR-image data, and the three sets of SR-images. Canopy-average spectral data were extracted and used to build predictive models for chlorophyll content. The evaluation results are summarized in Table 7. The model based on OH-image data achieved the highest prediction accuracy, with a validation coefficient of determination R_V^2 value of 0.88. By contrast, the model based on DLR-image data showed a substantial reduction

in prediction performance, with R_V^2 decreasing by 0.24 and RMSE increasing by 2.34 mg·L^{-1}, indicating the lowest estimation accuracy. This confirms that spatial resolution substantially affects chlorophyll estimation performance. Models based on SR-BA data showed improved prediction accuracy relative to the DLR-image model, whereas models based on SR-PM and SR-TM data showed further improvement. In particular, the prediction accuracy of the model based on SR-TM data processed using the T-UDAMSR approach reached a level comparable to that obtained with OH-image data, indicating effective restoration of chlorophyll estimation accuracy. The corresponding PLSR scatter plots are provided in Appendix Fig. S3.

Table 7
Evaluation results of chlorophyll content modeling using segmented data

Data source	R_C^2	R_V^2	RMSE (mg·L^{-1})
OH-image–Otsu	0.89	0.88	2.9
DLR-image–Otsu	0.77	0.64	5.24
SR-BA–Otsu	0.75	0.72	4.6
SR-PM–Otsu	0.86	0.82	3.64
SR-TM–Otsu	0.89	0.88	2.9

These results indicate that high-quality image data support more accurate chlorophyll content estimation. Among the evaluated methods, the proposed T-UDAMSR model achieved the best overall performance, effectively restoring chlorophyll estimation accuracy. This confirms that the trained model can mitigate accuracy degradation caused by reduced spatial resolution and demonstrates the feasibility of applying SR techniques to improve chlorophyll content detection.

5. Discussion

5.1. Testing generalization potential across different devices

To evaluate the generalization capability of the trained SR model at the near-ground scale, the model was applied to data acquired using the XIMEA XiQ multispectral camera. Super-resolved MSI and corresponding chlorophyll content measurements were then used to construct PLSR prediction models.

5.1.1 Data description and processing

Near-ground MSI data were collected as canopy images at a height of 1.6 m above ground using a XIMEA XiQ multispectral camera equipped with an Edmund Optics 16 mm/F1.4 VIS–NIR lens. Image acquisition was conducted between 11:00 and 13:00 on March 29, April 22, and May 10, 2021. For each campaign, 72 image sets were acquired, resulting in a total of 216 datasets. The MSI covered a spectral range of 600–875 nm with 25 channels, and the spatial resolution of each single-channel image was 406 pixels × 217 pixels.

Python and MATLAB R2022b were used to process the 216 multispectral datasets. The complete processing workflow is illustrated in Fig. 8(a) and is described as follows:

(1) The reflectance of each pixel in each spectral image was calculated using measurements from the reflectance calibration plate. The calibrated images were saved as 8-bit BMP files with a resolution of 409 pixels × 217 pixels and are referred to as original LR-images (OLR-images).

(2) The OLR-images with a resolution of 409 pixels × 217 pixels were input into the SR model, which generated MSI with a resolution of 1636 pixels × 868 pixels after SR. These outputs are referred to as super resolution image (SR-images).

(3) For each OLR-image, a ROI containing both crop canopy and soil with a size of 200 pixels × 100 pixels was cropped. For each corresponding SR-image, an ROI at the same spatial location with a size of 800 pixels × 400 pixels was extracted.

(4) The average reflectance of all pixels within each ROI was calculated. SAVI was then computed for each ROI and segmented using the Otsu algorithm to extract canopy reflectance. The resulting datasets are denoted as OLR-image-Otsu and SR-image–Otsu.

(5) Spectral data were preprocessed using the MSC algorithm, and samples were partitioned using the KS algorithm. A PLSR model relating spectral data to chlorophyll content was then established.

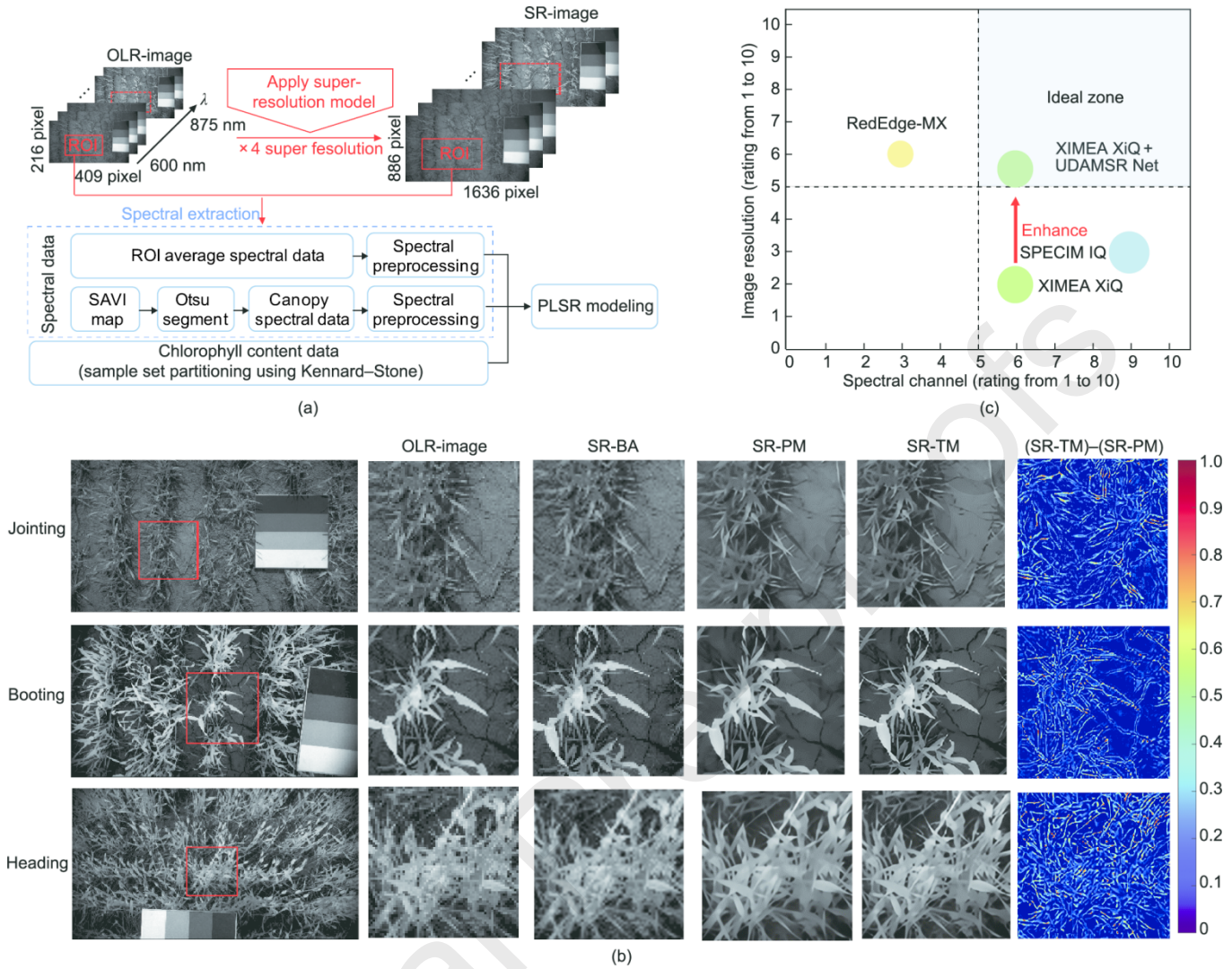

Fig. 8. Experimental workflow, comparison of SR results, and changes in sensor capability rating. (a) Experimental workflow. (b) Detail comparison of images before and after SR. (c) Migration of XIMEA XiQ camera performance. λ: wavelength.

5.1.2. Application results

Fig. 8(b) compares image details before and after SR for near-infrared (NIR) band images acquired at three growth stages from the same plot. In the OLR-images, wheat leaf edges appear blurred because of the LR, which complicates discrimination between canopy and background. Images processed using the bicubic algorithm show minimal enhancement and remain similar to the OLR-images, with indistinct leaf edges and considerable noise. In contrast, images generated using deep learning-based SR models exhibit substantial improvement. Compared with the P-UDAMSR outputs, the T-UDAMSR results show sharper leaf edges and clearer structural details. When the SR-TM images are subtracted from the SR-PM images and the differences are visualized using pseudo-color normalization, the main discrepancies are concentrated along leaf edges. This observation is consistent with previous results and confirms the superior performance of the T-UDAMSR model for multispectral wheat imagery.

PLSR prediction models were constructed using the extracted spectral data and measured chlorophyll content. The modeling results are summarized in Table 8. Regardless of whether background segmentation was applied, prediction accuracy improved after SR using the T-UDAMSR model. Compared with the corresponding pre-SR results, the coefficient of determination for R_C^2, increased by 0.07, and the coefficient of determination for R_V^2 increased by 0.14, reaching 0.83. At the same time, RMSE decreased to 3.51 mg·L^{-1}L. The corresponding PLSR scatter plots are provided in Appendix Fig. S4.

Table 8

Valuation results of PLSR prediction models for near-ground multispectral data.

Data source	R_C^2	R_V^2	RMSE
	0.82	0.69	4.68
OLR-image			
	0.80	0.72	4.50
SR-image			
	0.88	0.74	4.31
OLR-image–Otsu			
	0.89	0.83	3.51
SR-image–Otsu			

These results show that the TL-based SR model demonstrates strong generalization across different sensing devices. As illustrated in Fig. 8(c), after applying the proposed network, the performance of the XIMEA XiQ camera shifts from the lower-right region of the evaluation space into the IDEAL zone, indicating a marked improvement in effective sensing capability.

5.2. Testing generalization potential across spatial scales and geographic locations

Compared with near-ground data acquisition, UAV platforms provide efficient coverage over large areas. However, efficient UAV operation generally requires higher flight altitudes, which reduces the spatial resolution of acquired imagery. To address this limitation, the trained SR model was applied to UAV multispectral data to improve image quality and to evaluate its applicability at the UAV scale. Experiments were conducted in two experimental regions using different flight altitudes to assess spatial-scale and geographic generalization.

5.2.1 Data description and processing

UAV MSI were collected in two experimental regions using a DJI M600 Pro UAV equipped with multispectral sensors. In the Hengshui experiment, five-channel multispectral canopy images in the blue, green, red, red-edge, and NIR bands were acquired using a RedEdge-MX multispectral camera at a flight altitude of 50 m. In the Xinxiang experiment, the same five spectral bands were acquired using a MicaSense Altum multispectral camera at a flight altitude of 25 m.

Data processing was performed using PhotoScan, ENVI, ArcGIS, MATLAB R2022b, and Python. The overall workflow was similar to that used in the near-ground experiments, as illustrated in Fig. 9(a). The main difference at the UAV scale was the inclusion of image stitching and cropping. For each experiment, MSI were first stitched using PhotoScan. Subsequently, sign-centered ROIs were cropped using ENVI 5.6 and ArcGIS. In the Hengshui experiment, 216 ROIs with a size of 100 pixels × 100 pixels were extracted, whereas in the Xinxiang experiment, 216 ROIs with a size of 300 pixels × 300 pixels were extracted.

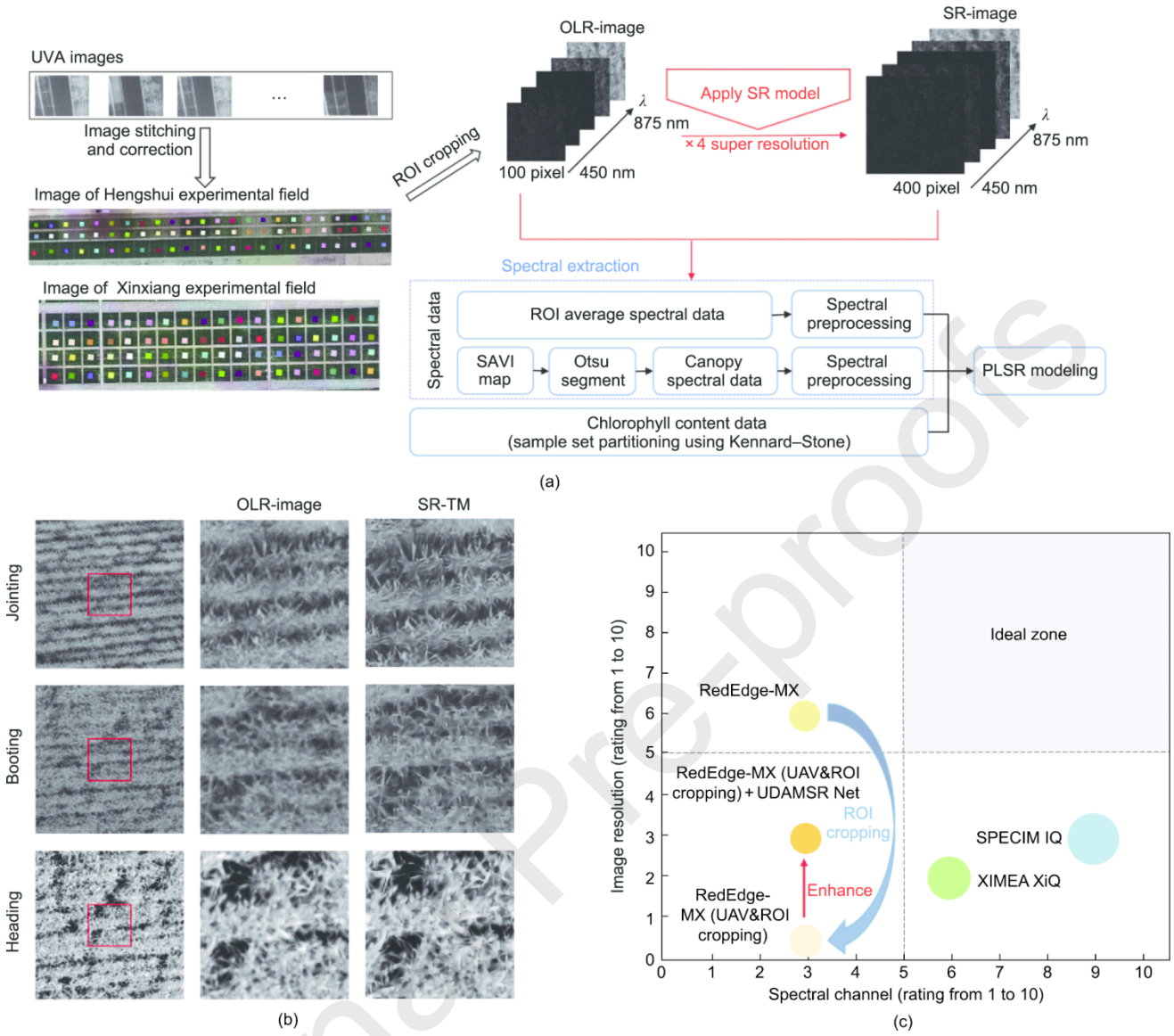

Fig. 9. UAV-scale experimental workflow, comparison of SR results, and changes in sensor capability rating. (a) UAV-scale experimental workflow. (b) Comparison of SR results. (c) Changes in sensor capability rating.

5.2.2. Application results

As shown in Fig. 9(b), which compares NIR band images from the same plot at three growth stages before and after SR, the SR-images exhibit sharper edges and finer structural details than the OLR-images.

The modeling results for the Hengshui experiment are summarized in the upper part of Table 9. Prediction accuracy improved consistently after applying the T-UDAMSR model. Before Otsu-based background segmentation, the SR-image data showed an increase in R_V^2 by 0.1 and a reduction in RMSE of 0.75 mg·L^{-1} compared with the OLR-image data. After segmentation, R_V^2 increased by 0.03 and RMSE decreased by 0.19 mg·L^{-1}.

The modeling results for the Xinxiang experiment show a similar trend, as presented in the lower part of Table 9. Chlorophyll content prediction accuracy improved after SR, with the best performance achieved for the segmented super-resolved data, yielding an R_V^2 value of 0.62. The corresponding PLSR scatter plots are provided in Appendix Fig. S5.

Table 9

Evaluation results of PLSR prediction models for UAV-scale multispectral data.

Study aera	Data source	R_C^2	R_V^2	RMSE

Hengshui experimental field	OLR-image	0.56	0.56	5.98
	SR-image	0.67	0.66	5.23
	OLR-image–Otsu	0.51	0.47	6.53
	SR-image–Otsu	0.54	0.50	6.34
Xinxiang experimental field	OLR-image	0.49	0.45	5.92
	SR-image	0.58	0.58	5.19
	OLR-image–Otsu	0.60	0.56	5.26
	SR-image–Otsu	0.62	0.62	4.92

These UAV-scale experiments further demonstrate that the trained model improves chlorophyll content prediction accuracy across different experimental regions. The results indicate that the proposed approach can be applied across multiple spatial scales and geographic locations with stable performance. In addition, consistent with near-ground experiments, application of the proposed network improves the effective sensing capability ratings of UAV-mounted multispectral devices.

5.3. Texture characterization of SR-images

Near-ground MSI data were used to examine texture characteristics before and after SR. The OLR-images were processed using the T-UDAMSR model, and texture features were extracted from images before and after SR. Five texture features were considered: angular second moment (ASM), entropy, contrast, homogeneity, and correlation. The results are summarized in Table 10. After SR, ASM increased and entropy decreased, indicating that image textures became more regular. At the same time, contrast decreased and homogeneity increased, suggesting effective noise suppression and smoother local texture patterns. To further validate these observations, OH-images were degraded to generate corresponding DLR-images, and the same texture features were extracted. The relationship between DLR-images and OH-images followed a pattern consistent with that observed between OLR-images and SR-TM images. These quantitative results confirm that SR processing improves texture regularity and image quality. Similar effects of texture enhancement have been reported in recent studies on remote sensing image processing [68,69], SR manufacturing [70], and point cloud feature recognition [71,72]. Visual comparisons are provided in Appendix Fig. S6, showing that SR-images appear clearer, smoother, and more structurally consistent.

Table 10
Image texture feature values for HR and LR-images.

Data	ASM	Entropy	Contrast	Correlation	Homogeneity
OLR-image(LR)	0.06	0.89	0.58	0.06	0.05
SR-TM(HR)	0.11↑	0.70↓	0.08↓	0.07 =	0.23↑
DLR-image(LR)	0.18	0.79	0.79	0.07	0.18
OH-image(HR)	0.21↑	0.69↓	0.22↓	0.07 =	0.21↑

5.4. Comparison between the original DASR and T-UDAMSR

A comparative experiment was conducted to evaluate differences between the original DASR model and the proposed T-UDAMSR model. High-spatial-resolution HSI and low-spatial-resolution MSI were used as experimental data. HSI were first downsampled, and the NIR channel was manually extracted from both the downsampled HSI and the MSI. The extracted NIR channel was duplicated to construct three-channel images compatible with the original DASR framework. SR reconstruction was then performed using both the original DASR and the T-UDAMSR models, with the outputs denoted as SR-3Channel and SR-TM, respectively. As shown in Fig. 10(a), the outputs generated by the original DASR model contain noticeable mesh artifacts, whereas the outputs from the T-UDAMSR model do not exhibit such artifacts. Quantitative comparisons based on hyperspectral data are presented in Fig. 10(b), which reports PSNR, RMSE, and SSIM values. Across all three image evaluation metrics, the T-UDAMSR model achieves better performance, demonstrating the effectiveness of the multi-channel modifications and the degradation-aware design.

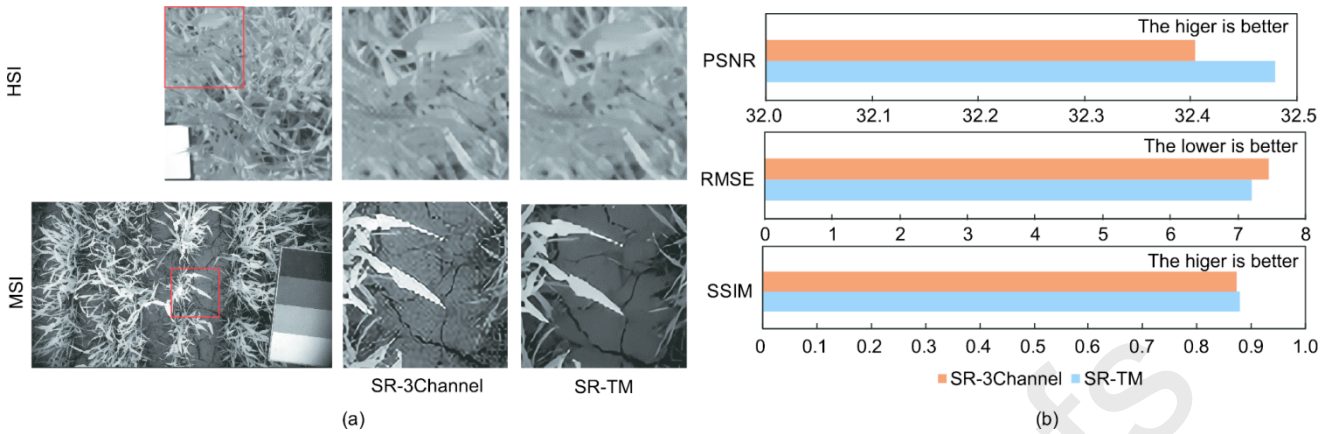

Fig. 10. Comparison of output results before and after multi-channel modification of the network. (a) Comparison of output images before and after multi-channel modification of the network. (b) Comparison of evaluation indices before and after multi-channel modification of the network.

5.5. Future work

Future work will focus on four main directions to further improve the applicability and robustness of the proposed method. These efforts are consistent with recent advances in agricultural vision [73], bionic sensors [74], image restoration techniques [75], optical system design [76], and robotic perception systems [77].

(1) We will systematically investigate the underlying causes of performance variation across different imaging devices and spatial scales. This analysis is expected to provide insight into model behavior under varying acquisition conditions and to support more effective deployment in practical applications.

(2) We will evaluate the generalization capability of the SR model across different crop types, such as maize and soybean, to assess transferability and performance in diverse agricultural scenarios.

(3) We will conduct multi-scale experiments using the same sensor to determine the maximum feasible detection distance that maintains acceptable accuracy. This investigation is essential for improving field-scale monitoring efficiency and supporting practical implementation.

(4) We will further examine the phenomenon observed in UAV-scale experiments, in which SAVI-based segmentation leads to reduced accuracy in PLSR models. Alternative segmentation strategies, including the use of multiple vegetation indices or learning-based segmentation approaches, will be explored to better preserve spectral variability and improve modeling performance.

6. Conclusions

This study proposes a novel unsupervised degradation-aware network for enhancing the spatial resolution of remote sensing images. Contrastive learning is applied to construct a degradation-aware network that improves model generalization. A multi-channel processing strategy is specifically designed to enable SR reconstruction for MSI and HSI. In addition, TL is adopted to address the limited availability of remote sensing SR datasets. Field experiments were conducted to collect data from different sensors, spatial scales, and experimental settings, and three groups of experiments were designed based on these datasets. The proposed network was trained and systematically evaluated in terms of SR performance, application effectiveness, and generalization capability. The results show that the trained T-UDAMSR model achieves strong performance in both image reconstruction and spectral consistency. By improving data quality, the model effectively increases the accuracy of chlorophyll content estimation. The generalization capability of T-UDAMSR was further examined using near-ground data acquired from different imaging devices and UAV-scale data collected across different geographic regions. The results demonstrate stable generalization across sensing equipment, spatial scales from near-ground to UAV, and geographic locations. Overall, this work establishes UDAMSR as a practical and efficient software-based solution that compensates for hardware limitations by reconstructing HR images from widely available LR data, thereby improving crop remote sensing analysis.

Acknowledgments

The project was supported by the National Key Research and Development Program: Strategic Science and Technology Innovation Cooperation key special project “Cooperative Research on AI-Enhanced Soil and Crop Sensing Technology”

(2025YFE0209000), the National Natural Science Fund of China (NSFC-FAPESP Project, W2412109), the Central Guidance Fund for Local Scientific and Technological Development Projects in Inner Mongolia (2024ZY0145), and the 2115 Talent Development Program of China Agricultural University. We would to acknowledge Dehua Gao, Lulu An, and Jinbo Qiao for their help with field data collection. We would like to acknowledge the field assistance of Mr. Junyong Ma from Institute of Dry Farming, Hebei Academy of Agriculture and Forestry Sciences; Professor Xiaojing Yan from the Institute of Plant Protection (IPP), Chinese Academy of Agricultural Sciences (CAAS).

Appendix A. Supplementary data

Supplementary data to this article can be found online.

References

[1] Morisse M, Wells DM, Millet EJ, Lillemo M, Fahrner S, Cellini F, et al. A European perspective on opportunities and demands for field-based crop phenotyping. Field Crop Res 2022;276:108371.

[2] Gao D, Li M, Zhang J, Song D, Sun H, Qiao L, et al. Improvement of chlorophyll content estimation on maize leaf by vein removal in hyperspectral image. Comput Electron Agr 2021;184:106077.

[3] Celis J, Xiao X, Wagle P, Basara J, McCarthy H, Souza L. A comparison of moderate and high spatial resolution satellite data for modeling gross primary production and transpiration of native prairie, alfalfa, and winter wheat. Agr Forest Meteorol 2024;344:109797.

[4] He L, Magney T, Dutta D, Yin Y, Köhler P, Grossmann K, et al. From the ground to space: using solar-induced chlorophyll fluorescence to estimate crop productivity. Geophys Res Lett 2020;47(7):e2020GL087474.

[5] Zhu J, Yin Y, Lu J, Warner TA, Xu X, Lyu M, et al. The relationship between wheat yield and sun-induced chlorophyll fluorescence from continuous measurements over the growing season. Remote Sens Environ 2023;298:113791.

[6] Barrett CB. Overcoming global food security challenges through science and solidarity. Am J Agr Econ 2021;103(2):422–47.

[7] Tilman D, Balzer C, Hill J, Befort BL. Global food demand and the sustainable intensification of agriculture. Proc Natl Acad Sci USA 2011;108(50):20260–4.

[8] Pan Y, Wang X, Zhang L, Zhong Y. E2EVAP: end-to-end vectorization of smallholder agricultural parcel boundaries from high-resolution remote sensing imagery. ISPRS J Photogramm Remote Sens 2023;203:246–64.

[9] Zhou G, Qian L, Gamba P. A novel iterative self-organizing pixel matrix entanglement classifier for remote sensing imagery. IEEE Trans Geosci Remote Sens 2024;62:1–21.

[10] Zhou G, Song N, Jia G, Wu J, Gao K, Huang J. Adaptive adjustment for laser energy and PMT gain through self-feedback of echo data in bathymetric LiDAR. IEEE Trans Geosci Remote Sens 2024;62:1–22.

[11] Xu X, Fu X, Zhao H, Liu M, Xu A, Ma Y. Three-dimensional reconstruction and geometric morphology analysis of lunar small craters within the patrol range of the Yutu-2 rover. Remote Sens 2023;15(17):4251.

[12] Zhang Z, Xu Y, Song J, Zou Q, Rasol J, Ma L. Planet craters detection based on unsupervised domain adaptation. IEEE Trans Aero Elec Sys 2023;59(5):7140–52.

[13] Yuan Y, Qin G, Li D, Zhou M, Shen YC, Ouyang Y. Real-time joint filtering of gravity and gravity gradient data based on improved Kalman filter. IEEE Trans Geosci Remote Sens 2024;62:1–12.

[14] Espejo-Garcia B, Mylonas N, Athanasakos L, Fountas S, Vasilakoglou I. Towards weeds identification assistance through transfer learning. Comput Electron Agr 2020;171:105306.

[15] Modi RU, Chandel AK, Chandel NS, Dubey K, Subeesh A, Singh AK, et al. State-of-the-art computer vision techniques for automated sugarcane lodging classification. Field Crop Res 2023;291:108797.

[16] Li B, Xu X, Zhang L, Han J, Bian C, Li G, et al. Above-ground biomass estimation and yield prediction in potato by using UAV-based RGB and hyperspectral imaging. ISPRS J Photogramm Remote Sens 2020;162:161–72.

[17] Liao Z, Dai Y, Wang H, Ketterings QM, Lu J, Zhang F, et al. A double-layer model for improving the estimation of wheat canopy nitrogen content from unmanned aerial vehicle multispectral imagery. J Integr Agr 2023;22(7):2248–70.

[18] Qiao L, Tang W, Gao D, Zhao R, An L, Li M, et al. UAV-based chlorophyll content estimation by evaluating vegetation index responses under different crop coverages. Comput Electron Agr 2022;196:106775.

[19] Tang W, Wang N, Zhao R, Li M, Sun H, An L, et al. Chlorophyll detector development based on snapshot-mosaic multispectral image sensing and field wheat canopy processing. Comput Electron Agr 2022;197:106999.

[20] Wang Y, Suarez L, Poblete T, Gonzalez-Dugo V, Ryu D, Zarco-Tejada PJ. Evaluating the role of solar-induced fluorescence (SIF) and plant physiological traits for leaf nitrogen assessment in almond using airborne hyperspectral imagery. Remote Sens Environ 2022;279:113141.

[21] Zhao R, Tang W, An L, Qiao L, Wang N, Sun H, et al. Solar-induced chlorophyll fluorescence extraction based on heterogeneous light distribution for improving in-situ chlorophyll content estimation. Comput Electron Agr 2023;215:108405.

[22] Xie Y, Plett D, Evans M, Garrard T, Butt M, Clarke K, et al. Hyperspectral imaging detects biological stress of wheat for early diagnosis of crown rot disease. Comput Electron Agr 2024;217:108571.

[23] Jia J, Chen J, Zheng X, Wang Y, Guo S, Sun H. Tradeoffs in the spatial and spectral resolution of airborne hyperspectral imaging systems: a crop identification case study. IEEE Trans Geosci Remote Sens 2022;60:1–18.

[24] Jia J, Zheng X, Wang Y, Chen Y, Karjalainen M, Dong S, et al. The effect of artificial intelligence evolving on hyperspectral imagery with different signal-to-noise ratio, spectral and spatial resolutions. Remote Sens Environ 2024;311:114291.

[25] Zhu Q, Guo X, Deng W, Shi S, Guan Q, Zhong Y, et al. Land-use/Land-cover change detection based on a Siamese global learning framework for high spatial resolution remote sensing imagery. ISPRS J Photogramm Remote Sens 2022;184:63–78.

[26] Kamei M. Effect of image resolution on automatic detection of whitefly (Hemiptera: Aleyrodidae) species on tomato leaflets using deep learning. Smart Agr Technol 2023;6:100372.

[27] Rocchini D. Effects of spatial and spectral resolution in estimating ecosystem α-diversity by satellite imagery. Remote Sens Environ 2007;111(4):423–34.

[28] Helfenstein IS, Schneider FD, Schaepman ME, Morsdorf F. Assessing biodiversity from space: impact of spatial and spectral resolution on trait-based functional diversity. Remote Sens Environ 2022;275:113024.

[29] Li M, Jia T, Wang H, Ma B, Lu H, Li S. AO-DETR: anti-overlapping DETR for X-Ray prohibited items detection. IEEE Trans Neur Net Lear 2025;36(7):12076–90.

[30] Wang W, Yin B, Li L, Li L, Liu H. A low light image enhancement method based on dehazing physical model. Comput Model Eng Sci 2025;143(2):1595–616.

[31] Xiao Y, Yuan Q, Jiang K, He J, Wang Y, Zhang L. From degrade to upgrade: Learning a self-supervised degradation guided adaptive network for blind remote sensing image super-resolution. Inform Fusion 2023;96:297–311.

[32] Ma X, Ding J, Sun H, Lu L, Cheng X, Zhang F, et al. A new computationally efficient algorithm to generate global fractional vegetation cover from Sentinel-2 imagery at 10 m resolution. Int J Digit Earth 2024;17(1):2344592.

[33] Li H, Xia J, Yang Z, Pan F, Liu Z, Liu Y. Meta-learning based domain prior with application to optical-ISAR image translation. IEEE Trans Circ Syst Vid 2024;34(8):7041–56.

[34] Zhou G, Liu W, Zhu Q, Lu Y, Liu Y. ECA-MobileNetV3(Large)+SegNet model for binary sugarcane classification of remotely sensed images. IEEE Trans Geosci Remote Sens 2022;60:1–15.

[35] Thomas C, Ranchin T, Wald L, Chanussot J. Synthesis of multispectral images to high spatial resolution: a critical review of fusion methods based on remote sensing physics. IEEE Trans Geosci Remote Sens 2008;46(5):1301–12.

[36] Sihvonen T, Duma Z, Haario H, Reinikainen S. Spectral profile partial least-squares (SP-PLS): local multivariate pansharpening on spectral profiles. ISPRS J Photogramm Remote Sens 2023;10:100049.

[37] Ma J, Yu W, Chen C, Liang P, Guo X, Jiang J. Pan-GAN: an unsupervised pan-sharpening method for remote sensing image fusion. Inform Fusion 2020;62:110–20.

[38] Xu H, Ma J, Shao Z, Zhang H, Jiang J, Guo X. SDPNet: a deep network for pan-sharpening with enhanced information representation. IEEE Trans Geosci Remote Sens 2021;59(5):4120–34.

[39] He J, Yuan Q, Li J, Xiao Y, Zhang L. A self-supervised remote sensing image fusion framework with dual-stage self-learning and spectral super-resolution injection. ISPRS J Photogramm Remote Sens 2023;204:131–44.

[40] Kong J, Ryu Y, Jeong S, Zhong Z, Choi W, Kim J, et al. Super resolution of historic Landsat imagery using a dual generative adversarial network (GAN) model with CubeSat constellation imagery for spatially enhanced long-term vegetation monitoring. ISPRS J Photogramm Remote Sens 2023;200:1–23.

[41] Yang D, Li Z, Xia Y, Chen Z. Remote sensing image super-resolution: challenges and approaches. In: Proceedings of the 2015 IEEE International Conference on Digital Signal Processing (DSP); 2015 Jun 21–24; Singapore City, Singapore. New York City: IEEE; 2015. p. 196–200.

[42] Lanaras C, Bioucas-Dias J, Galliani S, Baltsavias E, Schindler K. Super-resolution of Sentinel-2 images: learning a globally applicable deep neural network. ISPRS J Photogramm Remote Sens 2018;146:305-19.

[43] Lei S, Shi Z, Zou Z. Super-resolution for remote sensing images via local–global combined network. IEEE Geosci Remote Sens Let 2017;14(8):1243–7.

[44] Kim J, Lee JK, Lee KM. Accurate image super-resolution using very deep convolutional networks. In: Proceedings of the IEEE Conference on Computer Vision And Pattern Recognition (CVPR); 2016 Jun 27–30; Las Vegas, NV, USA. New York City: IEEE; 2016. p. 27–30.

[45] Lanaras C, Bioucas-Dias J, Galliani S, Baltsavias E, Schindler K. Super-resolution of Sentinel-2 images: learning a globally applicable deep neural

network. ISPRS J Photogramm Remote Sens 2018;146:305–19.

[46] Gu J, Sun X, Zhang Y, Fu K, Wang L. Deep residual squeeze and excitation network for remote sensing image super-resolution. Remote Sens 2019;11(15):1817.

[47] Dong X, Xi Z, Sun X, Yang L. Remote sensing image super-resolution via enhanced back-projection networks. In: Proceedings of the IGARSS 2020-2020 IEEE International Geoscience and Remote Sensing Symposium; 2020 Sep 26–Oct 2; Waikoloa, HI, USA. New York City: IEEE; 2021. p. 1480–3.

[48] Wang J, Shao Z, Huang X, Lu T, Zhang R, Ma J. Enhanced image prior for unsupervised remoting sensing super-resolution. Neural Networks 2021;143:400–12.

[49] Zhuang F, Qi Z, Duan K, Xi D, Zhu Y, Zhu H. A comprehensive survey on transfer learning. Pro IEEE. 2021;109(1):43–76.

[50] Zhao Z, Alzubaidi L, Zhang J, Duan Y, Gu Y. A comparison review of transfer learning and self-supervised learning: definitions, applications, advantages and limitations. Expert Syst Appl 2024;242:122807.

[51] Ma Y, Chen S, Ermon S, Lobell DB. Transfer learning in environmental remote sensing. Remote Sens Environ 2024;301:113924.

[52] Zhang Y, Hui J, Qin Q, Sun Y, Zhang T, Sun H, et al. Transfer-learning-based approach for leaf chlorophyll content estimation of winter wheat from hyperspectral data. Remote Sens Environ 2021;267:112724.

[53] Priyatikanto R, Lu Y, Dash J, Sheffield J. Improving generalisability and transferability of machine-learning-based maize yield prediction model through domain adaptation. Agr Forest Meteorol 2023;341:109652.

[54] Zhou J, Yang Q, Liu L, Kang Y, Jia X, Chen M, et al. A deep transfer learning framework for mapping high spatiotemporal resolution LAI. ISPRS J Photogramm Remote Sens 2023;206:30–48.

[55] Wang L, Wang Y, Dong X, Xu Q, Yang J, An W, et al. Unsupervised degradation representation learning for blind super-resolution. In: Proceedings of the IEEE/CVF Conference on Computer Vision and Pattern Recognition; 2021 Jun 20–25; Nashville, TN, USA. New York City: IEEE; 2021. p. 10581–90.

[56]Chen J, Song Y, Li D, Lin X, Zhou S, Xu W. Specular removal of industrial metal objects without changing lighting configuration. IEEE Trans Ind Inform 2024;20(3):3144–53.

[57] Wang Z, Zhang C, Chen Z, Hu W, Lu K, Ge L. ACR-Net: learning high-accuracy optical flow via adaptive-aware correlation recurrent network. IEEE Trans Circ Syst Vid 2024;34(10):9064–77.

[58] Tu B, Yang X, He B, Chen Y, Li J, Plaza A. Anomaly detection in hyperspectral images using adaptive graph frequency location. IEEE Trans Neur Net Lear 2025;36(7):12565–79.

[59] Wang L, Fu Q, Zhu R, Liu N, Shi H, Liu Z, et al. Research on high precision localization of space target with multi-sensor association. Opt Laser Eng 2025;184:108553.

[60] Chen J, Wang J, Wang J, Bai L. Joint fairness and efficiency optimization for CSMA/CA-based multi-user MIMO UAV Ad Hoc networks. IEEE J Sel Top Signal Process 2024;18(7):1311–23.

[61] He K, Fan H, Wu Y, Xie S, Girshick R. Momentum contrast for unsupervised visual representation learning. In: Proceedings of the IEEE/CVF

conference on computer vision and pattern recognition; 2020 Jun 13–19; Seattle, WA, USA. New York City: IEEE; 2020. p. 9726–35.

[62] He Q, Zhan J, Liu X, Dong C, Tian D, Fu Q. Multispectral polarimetric bidirectional reflectance research of plant canopy. Opt Laser Eng 2025;184:108688.

[63] Zhang R, Wang Y, Li Z, Ding F, Wei C, Wu M. Online adaptive keypoint extraction for visual odometry across different scenes. IEEE Robot Autom Let 2025;10(7):7539–46.

[64] Layati E, El Ghachi M. Oued Lakhdar watershed (Morocco), monitoring land use/cover changes: remote sensing and GIS approach. Geol Ecol Landsc 2025;9(4)1286–98.

[65] Li R, Wang Y, Sun S, Zhang Y, Ding F, Gao H. UE-extractor: a grid-to-point ground extraction framework for unstructured environments using adaptive grid projection. IEEE Robot Autom Let 2025;10(6):5991–8.

[66] Chen X, Jing R. Video super resolution based on deformable 3D convolutional group fusion. Sci Rep 2025;15(1):9050.

[67] Kruse FA, Lefkoff AB, Boardman JW, Heidebrecht KB, Shapiro AT, Barloon PJ, et al. The spectral image processing system (SIPS)—interactive visualization and analysis of imaging spectrometer data. Remote Sens Environ 1993;44(2):145–63.

[68] Chen G, Jia Y, Yin Y, Fu S, Liu D, Wang T. Remote sensing image dehazing using a wavelet-based generative adversarial networks. Sci Rep 2025;15(1):3634.

[69] Zhong F, Gao F, Liu T, Wang J, Sun J, Zhou H. Scattering characteristics guided network for ISAR space target component segmentation. IEEE Geosci Remote Sens Let 2025;22:1–5.

[70] Guan Y, Ding Y, Fang Y, Li J, Liu Y, Wang R, et al. Far-field femtosecond laser-driven λ/73 super-resolution fabrication of 2D van der Waals NbOI2 nanostructures in ambient air. Nat Commun 2025;16(1):4149.

[71] Cai H, Wang Y, Luo Y, Mao K. A dual-channel collaborative transformer for continual learning. Appl Soft Comput 2025;171:112792.

[72] Deng J, Liu S, Chen H, Chang Y, Yu Y, Ma W. A precise method for identifying 3-D circles in freeform surface point clouds. IEEE Trans Instrum Meas 2025;74:1–13.

[73] Jiang D, Wang H, Li T, Gouda MA, Zhou B. Real-time tracker of chicken for poultry based on attention mechanism-enhanced YOLO-Chicken algorithm. Comput Electron Agr 2025;237:110640.

[74] Ye Y, Lu Y, Su H, Tian Y, Jin S, Li G, et al. A hybrid bioelectronic retina-probe interface for object recognition. Biosens Bioelectron 2025;279:117408.

[75] Li L, Wang X, Huang D, He Y, Zhong Z, Xia Q. KEDM: knowledge-embedded diffusion model for infrared image destriping. IEEE Photonics J 2025;17(3):1–9.

[76] Wang S, Dong B, Xiong J, Liu L, Shan M, Koch AW, et al. Phase manipulating Fresnel lenses for wide-field quantitative phase imaging. Opt Lett 2025;50(8):2683–6.

[77] Gong L, Gao B, Sun Y, ZhangW, Lin G, Zhang Z. PreciseSLAM: robust, real-time, LiDAR–inertial–ultrasonic tightly-coupled SLAM with ultraprecise positioning for plant factories. IEEE Trans Ind Inform 2024;20(6):8818–27.

Declaration of Interest Statement

Dear editor:

No conflict of interest exits in the submission of this manuscript, and manuscript is approved by all authors for publication. I would like to declare on behalf of my co-authors that the work described was original research that has not been published previously, and not under consideration for publication elsewhere, in whole or in part. All the authors listed have approved the manuscript that is enclosed.

Thank you and best regards.

Yours sincerely,

Weijie Tang

Email: weijie@cau.edu.cn